

Doctoral Dissertation (Shinshu University)

Mechanical properties of polypropylene fiber
– Effects of primary structure parameters and
additive on the tensile and knot-pull strengths –

March 2021

Tatsuma Kunimitsu

Table of Contents

Chapter 1: General introduction

1. Polypropylene and polypropylene fiber
2. Study on the fiber strength
3. Effects of primary structures on mechanical properties
4. Knot-pull strength
5. Aim and objectives
6. Outline

Chapter 2: High strength fiber obtained from a high stereoregularity metallocene catalyst-synthesized polypropylene

1. Introduction
2. Experimental
 - 2.1. Polymers
 - 2.2. Spinning and drawing conditions
 - 2.3. Microscopy
 - 2.4. Tensile tests
 - 2.5. Thermomechanical and thermo properties measurements
 - 2.6. X-ray measurements
3. Results and discussion
 - 3.1. As-spun fibers
 - 3.2. Drawing
 - 3.3. Tensile Properties
 - 3.4. Creep at 125 °C
 - 3.5. Viscoelastic properties
 - 3.6. DSC analysis
 - 3.7. X-ray analyses
 - 3.8. Effects of molecular weight distribution
4. Conclusion

Chapter 3: High strength metallocene catalyst-synthesized polypropylene fibers with high stereoregularity and high molecular weight

1. Introduction
2. Experimental
 - 2.1. Polymer

- 2.2. Spinning and drawing conditions
- 2.3. Molecular weight
- 2.4. Microscopy
- 2.5. Tensile test
- 2.6. Thermomechanical analysis and differential scanning calorimetry
- 2.7. X-ray measurements
- 3. Results and discussion
 - 3.1. Thermal degradation during the melt spinning process
 - 3.2. Drawing
 - 3.3. Thermo-mechanical properties
 - 3.4. X-ray analyses
- 4. Conclusion

Chapter 4: Effects of draw ratio and additive on knot-pull breaking phenomenon in a polypropylene monofilament

- 1. Introduction
- 2. Experimental
 - 2.1. Sample
 - 2.2. Thermomechanical property measurements
 - 2.3. Tensile test
- 3. Result and discussion
 - 3.1. Drawing
 - 3.2. Mechanical properties
 - 3.3. Deformation behavior of the knot
 - 3.4. Fiber breaking mechanism of the knot
- 4. Conclusion

Chapter 5: Conclusions

Publications

Conferences

Acknowledgments

Chapter 1

General introduction

Chapter 1. General introduction

1. Polypropylene and polypropylene fiber

Polypropylene is a polymer that is classified into three stereoregularities: isotactic, syndiotactic, and atactic polypropylenes. Isotactic polypropylene (iPP), in which the methyl groups show the same steric configuration [1], is used mainly in polypropylenes [2].

The secondary structure of iPP is a threefold helix with a 0.65-nm chain axis repeat distance [3]. By packing this helical structure, iPP can form three crystal phases and a mesophase. The α -phase (monoclinic) is the most common crystal phase [4], and it is classified into $\alpha 1$ -(C2/c) and $\alpha 2$ -(P2₁/c) phases. The former is formed by low-temperature annealing of quenched iPP, and the latter is obtained by high-temperature annealing of $\alpha 1$ -phase [5]. β -phase (hexagonal) is formed by crystallization with a nucleant, such as *N,N'*-dicyclohexyl-naphthalene-2,6-dicarboxamide [6], and crystallization in a temperature gradient field [7] or shear field [8]. The γ -phase (orthorhombic) is formed by crystallization under high pressure [9] or by crystallization of the iPP random copolymer [10] or iPP of a short isotactic sequence [11]. The mesophase (smectic) is formed by the quenching of molten iPP [12], but the mesophase cannot be formed by iPP of less than the 0.680 isotactic pentad fraction [13].

The iPP is lightweight (density of 0.9 g/cm³) and hydrophobic (water absorption 24 h < 0.03%), and has a high tensile strength (35.5 MPa), high tensile modulus (1380 MPa), high flexural modulus (1690 MPa), good chemical resistance, and high dielectric strength (24–28 kV/mm) [14]. It also has a good melt processability with a melting temperature of 164 °C [4, 14]. Therefore, iPP is used mainly in injection-molded products, films, and fibers [4, 15].

The iPP is synthesized by raw-material refining, polymerization, aftertreatment, and granulation processes. Because impurities, such as water, oxygen, carbon monoxide, and carbonyl sulfide, affect the polymerization, they are eliminated from raw materials and auxiliary materials. The prepared raw material is contacted with catalyst for polymerization. After polymerization, the catalyst residue, solvent, unreacted propylene, and atactic polypropylene are eliminated from the iPP. Finally, obtained iPP is kneaded with additives and fillers, and pelletized [16].

The polymerization process is classified into three types: slurry, bulk, and vapor-phase polymerization. In slurry polymerization, propylene is polymerized in an inert hydrocarbon solvent. This process has been used in the earliest period of industrial iPP polymerization, but the energy cost was high because of solvent recovery after polymerization. To eliminate solvent recovery, bulk and vapor-phase polymerization were developed. This polymerization is carried out in liquefied propylene

and propylene gas, respectively. Vapor-phase polymerization has a higher energy efficiency because the propylene gas eliminates dry processing and increases the transfer speed. The energy efficiency of polymerization is affected by the catalyst performance. A high-activity and stereospecific catalyst can eliminate the removal of atactic polypropylene and catalyst residues [16, 17].

The iPP fiber is usually fabricated by melt spinning. The melt spinning system consists of an extruder that is equipped with a metering pump and spin pack, cooling chamber, spin finish oil application, godet rolls and winder. The source polymer, which is used in pellets or in granule form, is fed from the extruder hopper, and melt extruded through the spinneret. The flow rate of molten polymer is controlled by the metering pump. The typical extruded temperature is 230–280 °C with a typical spinneret diameter of 0.3–0.8 mm. The typical number of spinneret holes is 50–250 for the filaments, and 10000–50000 for staple fibers. Various spinneret hole shapes are used to control the fiber cross-sectional shape. The extruded polymer is cooled and solidified by air in the cooling chamber and taken up by the winder after oiling [18, 19].

Three types of iPP fiber—partially oriented yarn (POY), fully drawn yarn (FDY), and bulked continuous filament (BCF) yarn—have been manufactured. POY has been fabricated by one-step spinning with a take-up speed range of 2500–4000 m/min. A typical POY yarn of 40–200 dtex fineness has been used for textile application. FDY has been obtained by spinning and drawing. These processes are integrated (one-step process) or separated (two-step process). FDY has been fabricated by a one-step process, where the take-up speed was below 5000 m/min with a draw ratio of 3:1–8:1. An FDY of 50–300 dtex fineness has been used for textile application, and 500–2000 dtex has been used for industrial application. BCF yarn has been obtained by a one-step process of 600–1000 m/min spinning speed and 2200–3000 m/min take-up speed. After take-up, a three-dimensional crimp has been formed by a texturing jet. A BCF yarn of 150–3600 dtex fineness has been used for carpets and upholstery fabrics [20].

2. Study on the fiber strength

High-tensile strength fiber is thought to originate from the high molecular orientation and the high crystallinity [21]. During the fiber manufacture, molecular chains are mainly oriented during spinning and drawing, and the molecular orientation in the molten and solid states depends on the stress and draw ratio [22]. Because flexible polymers can be drawn up to a high draw ratio in the solid state, high tensile-strength fibers of these polymers tend to be obtained by drawing [23]. To increase

the draw ratio, the drawing method and heat source have been investigated. For example, the die drawing process, in which a heated polymer billet is drawn from a heated die by applying a pulling force on the billet at the exit side, resulted in the fabrication of a 16-times drawn polyoxymethylene fiber with a 700-MPa tensile strength [24]. Zone drawing that was carried out by localized heating and application of a high drawing stress fabricated a 7.2-times drawn poly(ethylene terephthalate) fiber with a 1.3-GPa tensile strength [25]. Microwave and CO₂ laser irradiation improved the drawability because both waves heated the fiber cross-section uniformly without contact. As a result, a 1.7-GPa strength polyoxymethylene fiber [21] and 0.96-GPa poly(ethylene terephthalate) fiber [26] were obtained by the former and latter methods, respectively.

The spinning condition affects the tensile strength of the drawn fiber. A lower take-up speed spun and drawn fiber had a higher tensile strength despite the almost equivalent drawing stress [27, 28]. The drawn fiber that was obtained by spinning with what is known as a melt structure control also had a high tensile strength [29]. The reported melt structure control methods were CO₂ laser irradiation in spin-line [30], nozzle diameter [31], conjugated spinning [32, 33], liquid isothermal bath [29, 34, 35] and spin-line drawing [29]. The poly(ethylene terephthalate) fiber that was obtained by CO₂ laser irradiation with a spin-line and small-diameter nozzle attained a tensile strength of 1.68 GPa [36]. An analysis and simulation of the molecular entanglement network in the fiber suggest that a more uniform entanglement network in the fiber was obtained by a low take-up speed spinning and melt structure control. This more uniform entanglement network is thought to apply the drawing stress evenly during drawing, and more molecular chains can bear the tensile stress [28, 29, 36].

Despite the various studies described above, however, the reported fiber tensile strengths are lower than the theoretical maximum tensile strengths [37]. This decrease in tensile strength is caused by defects, such as the molecular chain ends, molecular entanglement, molecular folds, microscale voids, and macroscale voids [38]. These defects can be somewhat eliminated by optimizing the fiber manufacturing processes and increasing the molecular weight [37, 38]. In particular, the study and simulation suggested that the fiber tensile strength was proportional to the weight average molecular weight to the power of 0.4 [39, 40] and 0.25 [41]. This result was explained by the decrease in number of chain ends that causes slippage between the molecules [37]. It has been reported that the decrease in number and orientation of the inter-microfibrillar tie chains that connect adjacent microfibrils decreases the tensile strength [28]. The increase in microfibril apparent elastic modulus was larger than that of the fiber tensile strength [42]. The number and orientation of the inter-microfibrillar tie

chains can be increased by the high drawing stress [28], and their number was increased by an increase in molecular weight [43].

3. Effects of primary structures on mechanical properties

Many types of primary-structure iPPs exist. The iPPs vary by molecular weight and molecular-weight distribution, and defects in the molecular chains affect the fiber mechanical properties. The increase in molecular weight decreases the number of chain ends but increases the melt viscosity and relaxation time. The high viscosity requires a high melt-spinning temperature, which tends to promote a decrease in molecular weight, and often reduces the effect of the high molecular weight [29].

The molecular-weight distribution is affected by catalyst type. Two types of catalysts exist; the Ziegler–Natta and metallocene catalysts are used mainly for iPP polymerization [20]. Ziegler–Natta-type catalysts are typically composed of transition-metal compounds with alkyls or hydrides, and tend to have multiple active sites (**Fig. 1.1 (a)**) [44, 45]. Contrary to the Ziegler–Natta type catalysts, metallocene-type catalysts are typically composed of compounds with two aromatic ring systems that are connected by a π -bonded metal atom that is treated with methylalumoxane, and has a single active site (**Fig. 1.1 (b)**) [46]. Because the molecular chain grows uniformly by a single active site, the metallocene catalyst can obtain a narrower molecular-weight distribution iPP than that of the Ziegler–Natta catalyst [20, 46].

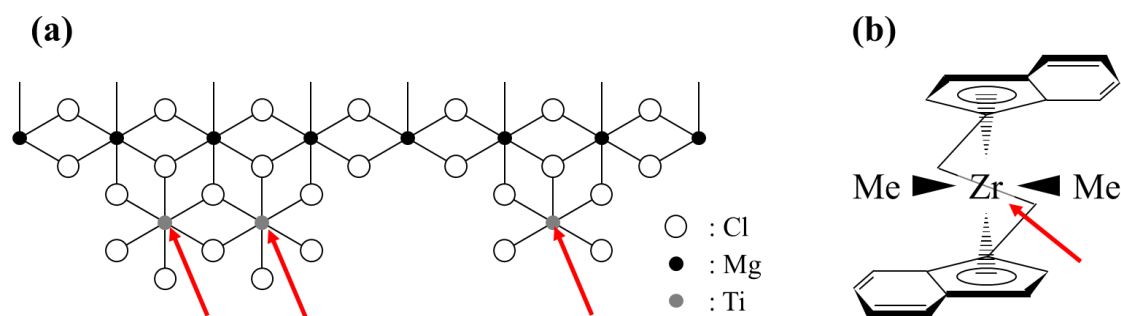


Fig. 1.1 Schemas of typical metallocene catalyst (a) and Ziegler–Natta catalysts (b). Active polymerization sites indicated.

The structural defects in molecular chains affect the mechanical properties of the fiber. Types of defects in molecular chains include the chain end, stereo-defect, and regio-defect (**Fig. 1.2**) [47]. The stereo-defect means a different steric configuration in the molecular chain, whereas the regio-defect

means a 2,1-insertion and 1,3-insertion. All defects decrease the crystallinity and melting temperature, but the regio-defect, which decreases the stereoregularity as occurs for the stereo-defects, reduces the melting temperature more than the stereo-defect at the same stereoregularity [48]. The metallocene catalysts iPP indicated a lower melting point than that of the Ziegler–Natta catalyst-synthesized iPP [48-52] because of its greater number of regio-defects. However, in recent years, a metallocene catalyst-synthesized iPP with an equivalent melting point to that of the Ziegler–Natta catalyst-synthesized iPP has been developed [53-57].

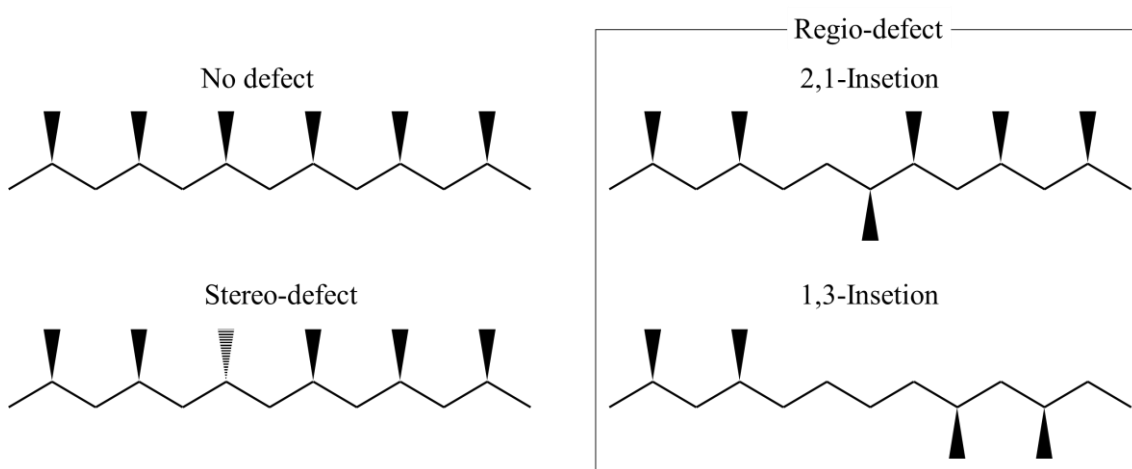


Fig. 1.2 Schemas of stereo and regio-defects of iPP.

The molecular-weight distribution and the structural defects of the chain affect the mechanical properties of the fiber and films. For example, it has been reported that their modulus increases with an increase in iPP isotacticity, the tensile strength was almost saturated above a 90% isotacticity [54, 58, 59]. The high molecular weight [60-63] and narrower molecular weight [51, 62-66] of the iPP increased the tensile strength of the fiber and film in general. However, Marcinčin et al. [50] reported a higher tensile strength fiber of the Ziegler–Natta catalyst-synthesized iPP compared with that of the metallocene catalyst-synthesized iPP despite the narrower molecular-weight distribution. This result was explained by the lower crystallinity, which was caused by the increased number of regio-defects of the metallocene catalyst-synthesized iPP compared with that of the Ziegler–Natta catalyst-synthesized iPP.

4. Knot-pull strength

Knot-pull strength—the tensile breaking stress of a knotted fiber—is one of the most important

fiber properties. It is often regarded as a more important property than tensile strength, particularly with regard to ships, fisheries, and civil engineering [67]. iPP monofilament, that is, a thick single fiber, is commonly used for these applications because it is highly flexible. The tensile strength of iPP fibers has increased recently, but their knot-pull strength has barely increased. This sluggish increase in the knot-pull strength has now become a critical problem.

The sluggish increase may be attributed to the complex breakage of knotted fibers. For example, the draw ratio at which the knot-pull strength reached a maximum is often lower than the draw ratio of the tensile strength maximum [68-70]. This indicates that a knotted fiber is not only broken by the tensile force but also by other forces, such as bending, compressional, twisting, shearing, and frictional forces applied to the knotted fiber [2, 71]. Yamaki explained the knot breakage mainly by the tensile force under the influence of radial compressional force [67], Pieranski et al. explained the knot breakage with computer simulations mainly by the bending force [72], and Uehara et al. interpreted the influence of twisting force on breakage [73]. Because the mechanism by which knotted fiber breaks is complex, the fiber breaking behavior also varies depending on the cross-sectional shape of the fiber or fiber bundle, the material, and the operating environment. The location of the fiber breakage varies, for example, most knotted fibers tend to break in the vicinity of the knot entrance [74], but fibers also break within the knot [69]. There have been many other studies on the breaking mechanism of knotted fibers. Konda et al. [75, 76] investigated the knot breaking mechanism using tensile stress-strain curves. They ignored the shearing and lateral compressional forces, and assumed that the fiber breaks according to the sum of the tensile and bending strains. Yabe suggested that a knotted fiber is broken by the weakest of three factors: the sum of the bending and frictional forces, the tensile strength under the influence of the radial compressional force, and the bending force that causes fiber buckling [69]. Fiber breakage with buckling has also been reported by Uehara et al. [73], Uddin et al. [77], and Lemstra et al. [78].

Various studies report on the increase in knot-pull strength. The high flexible nature of polymer fibers, such as iPP [79] and polyethylene [78], is suitable for knotting. The high knot-pull strength has been achieved by high-molecular-weight polymers [80]. Ultra-high-molecular-weight polyethylene fiber with a knot-pull strength of 12–20 cN/dtex has been manufactured industrially [81]. The new production techniques, such as high-temperature and high-stress annealing, sheath-core conjugated spinning, compositing with nanofiller, and meld blending between low compatibility polymers are also used to improve the knot-pull strength [77, 80, 82].

5. Aim and objectives

The tensile strength of high stereoregularity metallocene catalyst-synthesized iPP has been investigated in compression-molded films and for melt-spun and drawn fibers [54, 57]. However, the reported maximum strength of 3.5 cN/dtex (~310 MPa) is far less than that of commonly used iPP fibers [57]. This low strength is likely attributed to the low molecular orientation; that is, in the former cases, the strength was measured for a non-drawn sample, and the fiber was only drawn to 1.6 times in the latter case. In addition, the narrow-molecular-weight-distribution iPP reportedly suppresses the molecular weight decrease during melt-spinning [63]. This result suggests that high-molecular-weight metallocene catalyst-synthesized iPP likely increases the tensile strength. Therefore, the attainable maximum tensile strength of high-stereoregularity metallocene catalyst-synthesized iPP fiber was evaluated by optimizing the melt-spinning and drawing conditions. The fiber was taken up at a minimum stable spinning speed and the as-spun fiber was drawn in two steps to a maximum draw ratio at the drawable maximum temperature for each step. To verify the effects of stereoregularity, molecular weight, and its distribution on the mechanical properties of iPP fibers, six iPP types were investigated: iPP with a high stereoregularity and melt index of 4 and 20 g/10 min of metallocene catalyst-synthesized iPPs, a low stereoregularity with a melt index of 20 g/10 min metallocene catalyst-synthesized iPP, and a high stereoregularity with a melt index of 3, 4, and 20 g/10 min Ziegler–Natta catalyst-synthesized iPPs. All samples were spun and drawn under the same production conditions, and the attainable maximum tensile strength, initial modulus, high-temperature creep behavior, and fiber structure were compared.

A previous study has reported on the knot-pull strength improvement of iPP fibers via melt blending of the polyethylene component [82]. The report explained the improvement by the network structure that formed in the fiber. The knot-pull strength may be improved by slippage between incompatible components of polyethylene and iPP. We focused on the effect of an acrylic triblock copolymer additive on the knot-pull strength. This additive is usually used as an adhesive, compound, and resin modifier [83], and reportedly increases the toughness of the epoxy resin compounds by more than 20 times [84]. The additive is expected to improve the knot-pull strength because of the low compatibility between the additive and iPP [83]. To investigate the effect of additive and the draw ratio on the knot-pull strength of drawn iPP monofilaments (thick iPP single fibers), the knot-pull strength was compared with the tensile and loop strengths. The broken fiber ends after the loop and knot-pull tests were examined by scanning electron microscopy. The deformation behavior of the knot was

investigated by image processing a video that was obtained during the knot-pull test.

6. Outline

This study incorporates five chapters, with the contents summarized as follows.

In Chapter 2, the attainable tensile strength of a high stereoregularity metallocene catalyst-synthesized iPP was investigated. To analyze the effects of stereoregularity and molecular-weight distribution, low-stereoregularity metallocene catalyst-synthesized iPP and high-stereoregularity Ziegler–Natta catalyst-synthesized iPP were investigated.

In Chapter 3, the attainable tensile strength of a higher molecular weight and high stereoregularity metallocene catalyst-synthesized iPP was investigated. The obtained results were compared with the high-molecular-weight Ziegler–Natta catalyst-synthesized iPPs and low-molecular-weight iPPs.

In Chapter 4, knot breaking was investigated for the iPP monofilament (thick iPP single fiber) with and without an additive that comprised an acrylic triblock copolymer.

The study conclusions are provided in Chapter 5.

References

- [1] G. Natta, *Chem. Ind.* (1957) 1520–1530.
- [2] H. Endo, S. Ohira, K. Tashiro, *Seni binran* 3rd edition, Sen'i Gakkai Ed., Maruzen Publishing, pp. 55–56, 75 (2004). ISBN 978-4-621-07485-5.
- [3] B. Lotz, J.C. Wittmann, A.J. Lovinger, *Polymer*. 37 (1996) 4979–4992. doi:10.1016/0032-3861(96)00370-9.
- [4] E. P. Moore Jr., *Polypropylene handbook*, Kogyo Chosakai Publishing, pp. 143-171, 355, 356 (1998) ISBN 4-7693-4119-9.
- [5] M. Hikosaka, T. Seto, *Polym. J.* 5 (1973) 111–127. doi:10.1295/polymj.5.111.
- [6] J. Kotek, M. Raab, J. Baldrian, W. Grellmann, *J. Appl. Polym. Sci.* 85 (2002) 1174–1184. doi:10.1002/app.10701.S.
- [7] S.V. Meille, D.R. Ferro, S. Brückner, A.J. Lovinger, F.J. Padden, *Macromolecules*. 27 (1994) 2615–2622. doi:10.1021/ma00087a034.
- [8] J. Moitzi, P. Skalicky, *Polymer*. 34 (1993) 3168–3172. doi:10.1016/0032-3861(93)90385-N.
- [9] C. Nakafuku, *Polymer*. 22 (1981) 1673–1676. doi:10.1016/0032-3861(81)90384-0.
- [10] A. Turner-Jones, *Polymer*. 12 (1971) 487–508. doi:10.1016/0032-3861(71)90031-0.
- [11] C. De Rosa, F. Auriemma, T. Circelli, R.M. Waymouth, *Macromolecules*. 35 (2002) 3622–3629. doi:10.1021/ma0116248.
- [12] G. Natta, P. Corradini, *Nuovo Cim.* 15 (1960) 40–51. doi:10.1007/BF02731859.
- [13] T. Konishi, K. Nishida, T. Kanaya, K. Kaji, *Macromolecules*. 38 (2005) 8749–8754. doi:10.1021/ma050908f.
- [14] J. Brandrup, E.H. Immergut, E.A. Grulke, *Polymer Handbook* 4th edition, A John Wiley and Sons, 1999, pp. V/165. ISBN 0-471-481718-8.
- [15] G. Odian, *Principles of Polymerization* 4th edition, A John Wiley and Sons, pp.697, 698 (2004) ISBN 0-471-27400-3.
- [16] H. Sato, H. Ogawa, *Sumitomo Kagaku*. (2009) 1–11.
- [17] S. Nakamura, *Soc. Syst. Stud.* 28 (2014) 87–108. doi:10.34382/00003923.
- [18] T. Kikutani, *Sen'i Gakkaishi*. 59 (2003) P252–P258. doi:10.2115/fiber.59.P_252.
- [19] R. Kotek, M. Afshari, H. Avci, M. Najafi, *Polyolefin Fibres Structure Properties and Industrial Applications Second Edition*, Elsevier Inc., 2017, pp. 189–264. doi:10.1016/B978-0-08-101132-4.00007-2.
- [20] K. Schäfer, *Polypropylene*, Springer Netherlands, 1999, pp. 440–445. doi:10.1007/978-94-011-4421-6_61.

- [21] T. Kunugi, T. Ohta, K. Yabuki, High strength and high modulus fiber, Kyoritsu Shuppan, 1988, pp.6, 50, 51. ISBN 4-320-04233-6.
- [22] S. Arai et al., Plastic material in molding process, Morikita Publishing, pp.83 (2011) ISBN 978-4-627-66931-4.
- [23] M. Matsui, Sen'i Gakkaishi. 60 (2004) P166–P171. doi:10.2115/fiber.60.P_166.
- [24] A.K. Taraiya, M.S. Mirza, J. Mohanraj, D.C. Barton, I.M. Ward, J. Appl. Polym. Sci. 88 (2003) 1268–1278. doi:10.1002/app.11848.
- [25] T. Kunugi, A. Suzuki, T. Tsuki, Kobunshi Ronbunshu. 48 (1991) 703–710. doi:10.1295/koron.48.703.
- [26] T. Ikaga, A. Kobayashi, Y. Ohkoshi, Y. Gotoh, M. Nagura, Sen'i Gakkaishi. 58 (2002) 16–21. doi:10.2115/fiber.58.16.
- [27] R. Tomisawa, T. Ikaga, K.H. Kim, Y. Ohkoshi, K. Okada, H. Masunaga, T. Kanaya, M. Masuda, Y. Maeda, Polymer. 116 (2017) 367–377. doi:10.1016/j.polymer.2016.12.077.
- [28] R. Tomisawa, S. Oneda, T. Ikaga, K.H. Kim, Y. Ohkoshi, K. Okada, H. Masunaga, T. Kanaya, H. Katsuta, Y. Funatsu, Polymer. 164 (2019) 163–173. doi:10.1016/j.polymer.2019.01.002.
- [29] T. Kikutani, et al., Fundamental and Practical Technologies for Nano-Structured Polymeric Materials, CMC press, 2008, pp. 56-110, 271-321. ISBN 978-4-7813-0043-6.
- [30] M. Masuda, Y. Funatsu, K. Kazama, T. Kikutani, Sen'i Gakkaishi. 60 (2004) 338–344. doi:10.2115/fiber.60.338.
- [31] M. Masuda, W. Takarada, T. Kikutani, Sen'i Gakkaishi. 65 (2009) 118–126. doi:10.2115/fiber.65.118.
- [32] K. Nakata, Y. Ohkoshi, Y. Gotoh, M. Nagura, Y. Funatsu, T. Kikutani, Sen'i Gakkaishi. 60 (2004) 352–355. doi:10.2115/fiber.60.352.
- [33] K. Nakata, F. Nakamura, Y. Ohkoshi, Y. Gotoh, M. Nagura, A. Hamano, S. Takada, T. Kikutani, Int. Polym. Process. 27 (2012) 386–391. doi:10.3139/217.2573.
- [34] J.Y. Chen, P.A. Tucker, J.A. Cuculo, J. Appl. Polym. Sci. 46 (1992) 531–552. doi:10.1002/app.1992.070460320.
- [35] J.H. Yoon, H. Avci, M. Najafi, L. Nasri, S.M. Hudson, R. Kotek, Polym. Eng. Sci. 57 (2017) 224–230. doi:10.1002/pen.24406.
- [36] M. Masuda, W. Takarada, T. Kikutani, Int. Polym. Process. 25 (2010) 159–169. doi:10.3139/217.2330.
- [37] T. Ohta, Polym. Eng. Sci. 23 (1983) 697–703. doi:10.1002/pen.760231302.
- [38] T. Kikutani, J. Appl. Polym. Sci. 83 (2001) 559–571. doi:10.1002/app.2258.
- [39] P. Smith, P.J. Lemstra, J.P.L. Pijpers, J. Polym. Sci. Part A-2, Polym. Phys. 20 (1982) 2229–2241. doi:10.1002/pol.1982.180201206.
- [40] Y. Termonia, P. Meakin, P. Smith, Macromolecules. 18 (1985) 2246–2252.

doi:10.1021/ma00153a032.

- [41] M.A. Hallam, G. Pollard, I.M. Ward, *J. Mater. Sci. Lett.* 6 (1987) 975–976. doi:10.1007/BF01729888.
- [42] Y. Ohkoshi, M. Okazaki, T. Ikaga, K. H. Kim, K. Okada, H. Masunaga, H. Katsuta, Y. Funatsu, T. Kanaya, *Fiber Preprints, Japan (Annual Meeting)*. 74 (2020) 3B06.
- [43] Y. Otsuka, M. Nagata, T. Isshiki, K. Sugawara, T. Ikaga, K. H. Kim, Y. Ohkoshi, H. Katsuta, Y. Funatsu, K. Okada, T. Kabe, T. Kanaya, *Fiber Preprints, Japan (Autumn Meeting)*. 75 (2020) 1C19A.
- [44] P. Corradini, G. Guerra, L. Cavallo, *Acc. Chem. Res.* 37 (2004) 231–241. doi:10.1021/ar030165n.
- [45] T. Shiono, Y. Nakayama, Z. Cai, *Polymer synthesis*, Kodansha, 2010, pp. 756–782. ISBN 978-4-06-154362-1.
- [46] W. Kaminsky, A. Laban, *Appl. Catal. A Gen.* 222 (2001) 47–61. doi:10.1016/S0926-860X(01)00829-8.
- [47] M. Gahleitner, J. R. Severn, *Tailor-made polymers: via immobilization of alpha-olefin polymerization catalysts*, Wiley-VCH, 2008, pp. 1–42. ISBN: 978-3-527-31782-0
- [48] T. Tsutsui, N. Ishimaru, A. Mizuno, A. Toyota, N. Kashiwa, *Polymer*, 30, 1350–1356 (1989). doi:10.1016/0032-3861(89)90059-1.
- [49] E.B. Bond, J.E. Spruiell, J.S. Lin, *J. Polym. Sci. B Polym. Phys.* 37 (1999) 3050–3064. doi:10.1002/(SICI)1099-0488(19991101)37:21<3050::AID-POLB14>3.0.CO;2-L.
- [50] E.B. Bond, J.E. Spruiell, *J. Appl. Polym. Sci.* 82 (2001) 3223–3236. doi:10.1002/app.2181.
- [51] E.B. Bond, J.E. Spruiell, *J. Appl. Polym. Sci.* 82 (2001) 3237–3247. doi:10.1002/app.2182.
- [52] A. Marcinčin, A. Ujhelyiová, K. Marcinčin, M. Hricová, *J. Therm. Anal. Calorim.* 123 (2016) 1329–1341. doi:10.1007/s10973-015-4991-4.
- [53] W. Spaleck, F. Kuber, A. Winter, J. Rohrmann, B. Bachmann, M. Antberg, V. Dolle, E.F. Paulus, *Organometallics*. 13 (1994) 954–963. doi:10.1021/om00015a032.
- [54] C. De Rosa, F. Auriemma, G. De Lucia, L. Resconi, *Polymer*. 46 (2005) 9461–9475. doi:10.1016/j.polymer.2005.07.028.
- [55] K. Koike, Y. Ohkoshi, K.H. Kim, T. Ikaga, K. Toyoda, T. Kunimitsu, Japan Patent, Prime Polymer Co. Ltd., Shinshu Univ., Mitsui Chemicals Inc., (2017) WO2017/209283.
- [56] K. Koike, Y. Ohkoshi, K. H. Kim, T. Ikaga, T. Kunimitsu, S. Warashina, Japan Patent, Prime Polymer Co., Ltd., Shinshu University, Mitsui Chemicals Inc., (2019) P2019-99983 A.
- [57] R. Xu, P. Zhang, H. Wang, X. Chen, J. Xiong, J. Su, P. Chen, Z. Zhang, *Polymers*. 11 (2019) 1–17. doi:10.3390/polym11040729.
- [58] J.E. Spruiell, F.M. Lu, Z. Ding, G. Richeson, *J. Appl. Polym. Sci.* 62 (1996) 1965–1975. doi:10.1002/(SICI)1097-4628(19961212)62:11<1965::AID-APP21>3.0.CO;2-W.

- [59] T. Takahashi, Y. Tsurunaga, T. Kondo, *J. Appl. Polym. Sci.* 130 (2013) 981–988. doi:10.1002/app.39260.
- [60] W.C. Sheehan, T.B. Cole, *J. Appl. Polym. Sci.* 8 (1964) 2359–2388. doi:10.1002/APP.1964.070080528.
- [61] K. Kamide, *Sen'i Gakkaishi*. 26 (1970) 1–10. doi:10.2115/fiber.26.1.
- [62] E. Andreassen, O.J. Myhre, E.L. Hinrichsen, K. Grøstad, *J. Appl. Polym. Sci.* 52 (1994) 1505–1517. doi:10.1002/app.1994.070521015.
- [63] S. Misra, F.-M. Lu, J.E. Spruiell, G.C. Richeson, *J. Appl. Polym. Sci.* 56 (1995) 1761–1779. doi:10.1002/app.1995.070561307.
- [64] F.-M. Lu, J.E. Spruiell, *J. Appl. Polym. Sci.* 34 (1987) 1521–1539. doi:10.1002/app.1987.070340415.
- [65] Z.T. Mazraeh-Shahi, M.R.M. Mojtahedi, *J. Text. Inst.* 101 (2010) 547–555. doi:10.1080/00405000802597600.
- [66] S. Ota, Japan Patent, UbeNitro Kasei Co. Ltd., 2001, P2001-123322A.
- [67] K. Yamaki, *Journal of the Textile Machinery Society*. 18 (1965) 356–361. doi:10.4188/transjtmsj1948.18.356.
- [68] Y. Hori, *Kobunshi*. 11 (1962) 150–155. doi:10.1295/kobunshi.11.150.
- [69] H. Yabe, *Journal of Chugoku Junior College*. 18 (1987) 1–8.
- [70] H. Endo, S. Ohira, *Sen'i Gakkaishi*. 47 (1991) P333–P335. doi:10.2115/fiber.47.6_P333.
- [71] R. Oono, *Journal of Home Economics of Japan*. 47 (1996) 461–468. doi:10.11428/jhej1987.47.461.
- [72] P. Pieranski, S. Kasas, G. Dietler, J. Dubochet, A. Stasiak, *New J. Phys.* 3 (2001) 10.1–10.13. doi:10.1088/1367-2630/3/1/310.
- [73] H. Uehara, H. Kimura, A. Aoyama, T. Yamanobe, T. Komoto, *New J. Phys.* 9 (2007) 65. doi:10.1088/1367-2630/9/3/065.
- [74] C. W. Ashley, *The Ashley Book of Knots*, Faber and Faber, 1944, pp. 17. ISBN 978-0571096596.
- [75] A. Konda, C. Koyama, T. Agatsuma, *Bulletin of the Textile Research Institute* 62 (1962) 25–29.
- [76] A. Konda, S. Sekiguchi, T. Misaizu, K. Shirakashi, *Sen'i Kikai Gakkaishi*. 27 (1974) T127–T135. doi:10.4188/transjtmsj.27.8_T127.
- [77] A. J. Uddin, J. Araki, Y. Gotoh, *Biomacromolecules*. 12 (2011) 617–624. doi:10.1021/bm101280f.
- [78] P. J. Lemstra, R. Kirschbaum, T. Ohta, H. Yasuda, *Developments in Oriented Polymers-2*, I. M. Ward Ed., Elsevier applied science, 1987, pp. 69–72. ISBN 978-1-85166-045-2.
- [79] M. Ahmed, *Polypropylene fibers – Science and Technology*, Elsevier, 1982, pp. 653. ISBN 0-

444-42090-8.

- [80] S. Oohira, S. Hashimoto, Y. Kokuno, *Seikei-Kakou*. 13 (2001) 280-284.
- [81] Y. Ohta, *Sen'i Gakkaishi*. 66 (2010) P91–P97. doi:10.2115/fiber.66.P_91.
- [82] Y. Atarashi, Some Mechanical Properties of Polyethylene-Polypropylene Blend Fibers, *Sen'i Gakkaishi*. 27 (1971) 204–210. doi:10.2115/fiber.27.204.
- [83] T. Ono, *Journal of The Adhesion Society of Japan*. 52 (2016) 342–347. doi:10.11618/adhesion.52.342.
- [84] H. Kishi, Y. Kunimitsu, J. Imade, S. Oshita, Y. Morishita, M. Asada, *Polymer*. 52 (2011) 760–768. doi:10.1016/j.polymer.2010.12.025.

Chapter 2

High strength fiber obtained from a high
stereoregularity metallocene catalyst-
synthesized polypropylene

Chapter 2: High strength fiber obtained from a high stereoregularity metallocene catalyst-synthesized polypropylene

1. Introduction

In this Chapter, the attainable maximum tensile strength of new metallocene catalyst-synthesized isotactic polypropylene (iPP) fiber was evaluated based on optimization of the melt-spinning and drawing conditions. The fiber was taken-up at the minimum stable spinning speed and the as-spun fiber was two-step drawn to the maximum draw ratio at the drawable maximum temperature for each step. To verify the effects of stereoregularity and molecular weight distribution on the structure, thermal properties and mechanical properties of iPP fibers, besides the new metallocene catalyst-synthesized iPP (m98), a low stereoregularity metallocene catalyst-synthesized iPP (m93) having the same molecular weight distribution of m98, and Ziegler–Natta catalyst-synthesized iPP (ZN98) having the same stereoregularity and melting point of m98 were also investigated. All samples were spun and drawn under the same production conditions, and the attainable maximum tensile strength, initial modulus, high temperature creep behavior, and fiber structure were compared.

2 Experimental

2.1 Polymers

Three types of iPPs were examined in this study; high-stereoregularity iPP polymerized by metallocene (m98) and Ziegler–Natta catalysts (Grade Y2000GV: ZN98), and low-stereoregularity iPP polymerized by a metallocene catalyst (m93). All polymers were supplied by Prime Polymer Co., Ltd. (Tokyo, Japan). **Table 2.1** shows the characteristics of each polymer [1].

2.2 Spinning and drawing conditions

Source polymers were melt-extruded from a BT-30-S 2-42-L twin-screw extruder (Research Laboratory of Plastics Technology Co., Ltd., Tokyo, Japan) through the spinneret of 0.7 mm diameter (D_s) and 2.1 mm length. The spinning conditions are listed in **Table 2.2**. The melt draw ratio (MDR) was calculated from Eq. 2.1 assuming a iPP density (ρ) of 0.9 g/cm³ [2].

$$\text{MDR} = \frac{D_s^2}{D_{\text{calc}}^2} = \frac{\pi \rho v}{4W} D_s^2 \quad (2.1)$$

The melt-extruded polymers were quenched by a 20 °C-water bath at a distance of 78 cm from the spinneret. As-spun fibers were continuously drawn to the certain ratio by the speed difference between the feed and take-up rollers (1st-step drawing). The fiber drawn 10 times at the 1st-step drawing was also drawn again to a certain ratio (2nd-step drawing). The feed speed was fixed at 1

m/min, and a hot plate heater with a 225-mm contact length was used for both drawing steps. The drawing tension and the fiber diameter (D_{obs}) were measured in situ by a tension meter (HS-1500S, Eiko Sokki Co., Ltd.) equipped with a 100 gf pickup sensor, and outer diameter detector (LS-7010, Keyence Co., Ltd.), and captured at a sampling period of 100 ms by a data logger (NR-2000, Keyence Co., Ltd.). The drawing stress was calculated from the obtained tension and the fiber fineness, which was measured by a denier tester (Denicon DC-21, Search Co., Ltd.), and averaged for 12 fiber samples.

2.3 Microscopy

The birefringence of the fiber was measured at room temperature with a polarized microscope (BX51-33POC, Olympus Co., Ltd.) with a halogen lamp light source. Tricresyl phosphate was used as the immersion oil. The average and standard deviation of the birefringence were calculated for 10 samples. The broken fiber edge after the tensile test was observed by a scanning electron microscope (SEM, VE9800/8800, Keyence Co., Ltd.).

Table 2.1 Materials [1]

Polymer	Catalyst	Mw	Mn	Mw/Mn	Mz/Mw	*IPF	Regio defect		**MI	T_m
						(mmmm)	2,1- insertion	1,3- insertion		
						(%)	(%)	(%)	(g/10min)	(°C)
m98	metallocene	176,000	70,000	2.5	1.8	98	0.0	Not Detected	20	162
m93	metallocene	177,000	71,000	2.5	1.9	93	0.0	0.1	20	147
ZN98	Ziegler- Natta	214,000	61,500	3.5	2.4	98	Not Detected	Not Detected	20	162

*Isotactic pentad fraction, **melt index.

Table 2.2 Spinning conditions and diameter of the as-spun fibers

Spinning Conditions	Cooling	Melt Draw Ratio	Mass Flow	Take-up	Spinning	Estimated Fiber Diameter (D_{calc})
			Rate (W)	Speed (v)	Temperature	
			(g/min)	(m/min)	(°C)	(μ m)
LW	Water	14.4	1.5	62.5	260	184
LA	Air	14.4	3.0	125	220	184
HA	Air	116	3.0	1000	240	65

2.4 Tensile tests

Tensile testing was performed at room temperature with the use of an Autograph AGS-X instrument (Shimadzu Co., Ltd.) equipped with a 50-N load cell and air chuck. The initial length was 40 mm, and the elongation rate was 100 mm/min for the as-spun fibers and 40 mm/min for the drawn fibers. The strength and initial modulus determined from the nominal stress nominal strain curve were averaged for 12 samples. The initial modulus was calculated from the strain range of 0.13%–1.8%. Fineness (F) was used for the stress because of its high accuracy. The fineness of the drawn fibers was measured by the method described in Section 2.2, and the fineness of the as-spun fiber was estimated from the fiber diameter by assuming a fiber density of 0.9 g/cm³ [2]. The fiber diameter was measured by a digital microscope (Keyence VHX-1000).

2.5 Thermomechanical and thermo properties measurements

The creep behavior at 125 °C was measured by a thermomechanical analyzer (SII Nanotechnology Co., Ltd. SS6100 thermal analysis rheology system). The sample length was 10 mm and the applied stress was 50 MPa. The dynamic viscoelastic behavior was measured on a ITK-DVA25 (IT Keisoku Seigyo, Co., Ltd). The temperature was raised from room temperature to 200 °C at 10 K/min, and the storage modulus and loss modulus were recorded every 1 K. The sample length was 25 mm and the measurement frequency was 10 Hz. Differential scanning calorimetry (DSC) was performed with the use of a ThermoplusDSC8230 (Rigaku Co., Ltd.) from room temperature to 200 °C at 10 K/min. Approximately 2 mg of cut fiber sample was enclosed in an aluminum pan. Nitrogen gas was flowed at 50 mL/min during the measurement. The melting peak temperature (T_m) and the difference between the heat of fusion and the heat of cold crystallization (ΔH_m) were determined from the DSC curve. The crystallinity (X_{DSC}) was calculated from Eq. 2.2 assuming ΔH_m^0 of 209 kJ/kg [3].

$$X_{DSC} = \frac{\Delta H_m}{\Delta H_m^0} \quad (2.2)$$

2.6 X-ray measurements

Wide-angle X-ray diffraction (WAXD) and small-angle X-ray scattering (SAXS) images were captured by RA-Micro7 / R-AXIS-IV ++, and NanoViewer / PILATUS 100K detectors (Rigaku Co., Ltd.) systems. For WAXD and SAXS measurements, camera lengths of 250 and 1380 mm and exposure times of 10 and 60 min, were used respectively. The X-ray source for the measurements was Cu-K α generated at a tube voltage of 40 kV and tube currents of 20 and 30 mA. A one-directional aligned fiber bundle was used as the specimen, having a width of 3 mm and thickness of 150 μ m.

3 Results and discussion

3.1 As-spun fibers

WAXD images of as-spun fiber are shown in **Fig. 2.1**. The α -crystal diffraction features were observed for air-cooled spun fibers (LA, HA); however, no crystal diffraction features were observed for the water-quenched spun fiber (LW) but rather mesophase diffraction features appeared [4]. These results agree with previous reports [4] that the quenching of a molten polymer promotes mesophase development. The low-MDR fibers, metallocene catalyst-synthesized iPP (m98 and m93) had an a^* -axis orientation, whereas Ziegler–Natta catalyst-synthesized iPP (ZN98) had almost no orientation, and the a^* -axis and c -axis orientations were mixed for all high MDR fibers. As the molecular orientation increased, following the a^* -axis of iPP crystal first aligning to the fiber axis, the c -axis of the iPP crystal alternately tended to align to the fiber axis. Hence, the α -crystals in metallocene catalyst-synthesized iPP fibers had a greater tendency to orient along the fiber axis than the crystals in Ziegler–Natta catalyst-synthesized iPP fibers spun at the same MDR.

Polarized microscope images are shown in **Fig. 2.2**. Air-cooled spun fibers (LA, HA) appeared slightly cloudy, whereas the water-quenched spun fibers (LW) were transparent. The cloudiness is attributed to scattering from particles, which are likely spherulites. In particular for the LA fibers, the particle size of the Ziegler–Natta catalyst-synthesized iPP (ZN98) fiber was larger than that of metallocene catalyst-synthesized iPP (m98 and m93). The obtained birefringence (**Fig. 2.3**) increased as the MDR increased, decreased through water-quenching, and increased in order of $\text{ZN98} < \text{m98} < \text{m93}$. It has been reported that the birefringence of wider molecular weight distribution iPP increases on the melt-spinning-line more rapidly after extrusion from the spinneret than that of narrower molecular weight distribution iPP [5, 6], which suggests that Ziegler–Natta catalyst-synthesized iPP (ZN98) solidified at the higher temperature. This result might explain the lower crystal orientation and molecular orientation of the Ziegler–Natta catalyst-synthesized iPP fiber and the spherulite growth in the spinning-line after high-temperature solidification. Conversely, the transparency of the LW fibers indicates that no spherulites formed in the fiber, which agrees with the WAXD results. The lower crystallinity caused by water quenching and the lower spinning stress of the higher spinning temperature likely introduces a low birefringence into the LW fibers.

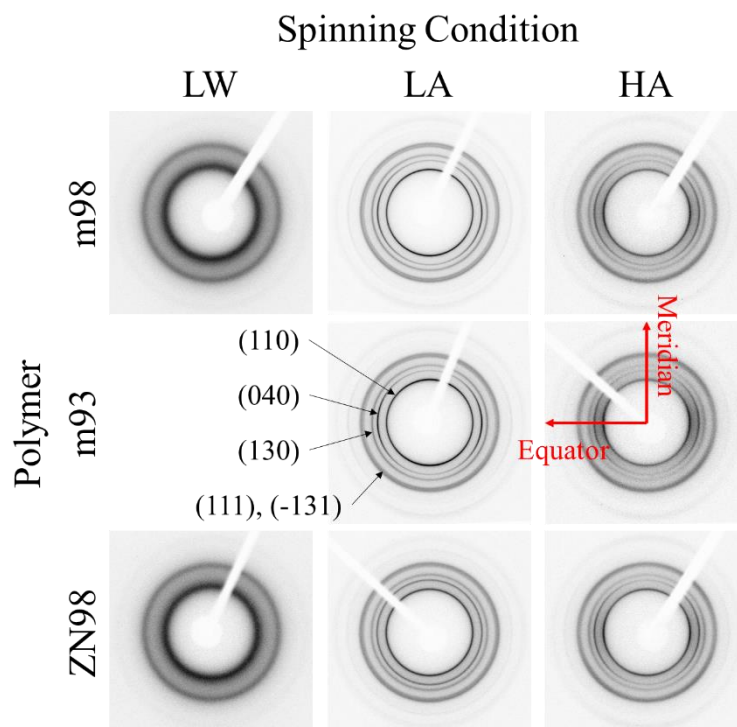


Fig. 2.1 Wide angle X-ray diffraction images of as-spun fibers. Polymers (m98, m93, and ZN98) and spinning conditions (LW, LA, and HA) are shown in the figure.

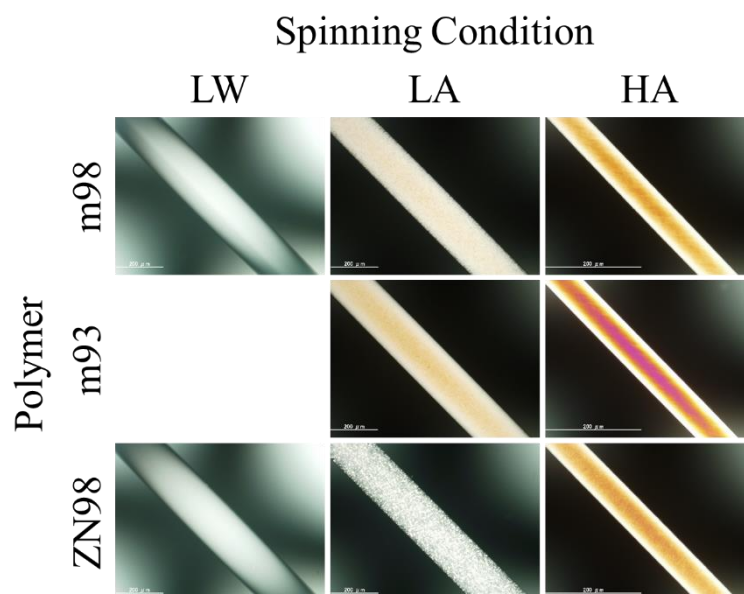


Fig. 2.2 Polarization microscope images of as-spun fibers. Polymers (m98, m93, and ZN98) and spinning conditions (LW, LA, and HA) are shown in the figure.

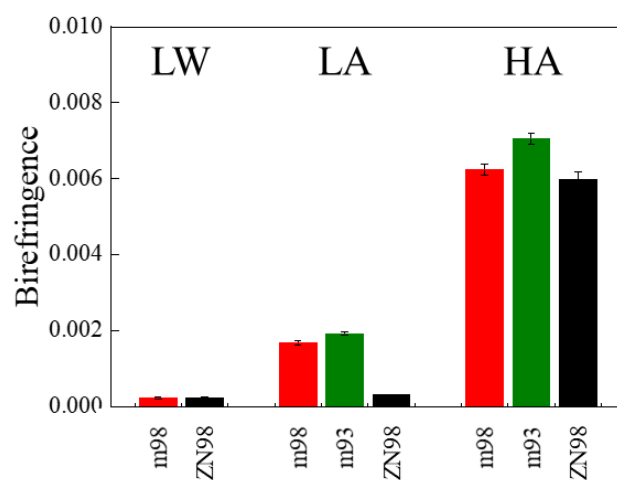


Fig. 2.3 Birefringence of as-spun fibers of m98, m93, and ZN98. Each fiber was spun at MDR14.4 (L) or MDR116 (H) with cooling by air (A) or quenching by water (W).

3.2 Drawing

To compare the attainable maximum tensile strength of the fibers obtained from each polymer, each fiber was drawn to the maximum draw ratio at the attainable maximum drawing temperature of each polymer fiber. By increasing the heater temperature in 5-K steps, the low stereoregularity iPP (m93) fibers fused over 125 and 155 °C for the 1st and 2nd step drawing, respectively, whereas the high stereoregularity iPP (m98 and ZN98) fibers fused over 140 and 175 °C. Therefore, these temperatures were selected as the drawing temperature for each polymer and each step drawing.

The obtained drawing stresses are shown in **Fig. 2.4**. At the same draw ratio for both 1st- and 2nd-step drawing, the drawing stress of the m93 fiber was the greatest among three. The drawing stress of the m98 fibers was somewhat greater than those of ZN98 for low MDR fibers, in particular at a higher draw ratio; however, the opposite result was obtained for high MDR (HA) fibers. The fiber whitening draw ratios are indicated in the figure. Moreover, the maximum draw ratio shown in the figure indicates the maximum draw ratio at which the fiber could be drawn stably for more than 10 min. Low stereoregularity iPP (m93) had the lowest whitening draw ratio and smallest maximum draw ratio but the greatest whitening drawing stress. Conversely, there were no significant differences in the whitening and maximum draw ratios between m98 and ZN98. Thus, at least for the air-cooled spun fibers (LA), the maximum applicable drawing stress for metallocene catalyst-synthesized (m98) fiber was clearly greater than that for the Ziegler–Natta catalyst-synthesized iPP with same stereoregularity (ZN98) fibers.

The observed fiber diameter D_{obs} results are listed in **Table 2.3**. The observed diameter of the as-spun fiber was almost equal to the fiber diameter D_{calc} (**Table 2.1**), as calculated from the spinning conditions. However, for fibers drawn at high draw ratios, the observed diameter appeared to be larger than that calculated from D_{calc} and the draw ratio λ . This difference in fiber diameter is attributed to void formation because the crystallinity of the drawn fibers obtained by both DSC and WAXD did not differ greatly, as shown in **Table 2.3**. The void fraction V was estimated from Eq. 2.3 [7, 8] assuming that the diameter difference was caused by voids.

$$V = 1 - \frac{1}{\lambda} \left(\frac{D_{\text{calc}}}{D_{\text{obs}}} \right)^2 \quad (2.3)$$

The obtained void fractions are shown in **Fig. 2.5**. The void fraction began to increase over the whitening draw ratio, and the two-step drawn low stereoregularity iPP (m93) fiber had a larger void fraction than those of the high stereoregularity iPP (ZN98 and m98) fibers drawn at the same draw ratio. The void fraction estimated by this method did not consider the void size; however, contributions of macroscale voids larger than the visible light wavelength should dominate the void fraction increase of the whitening draw ratio.

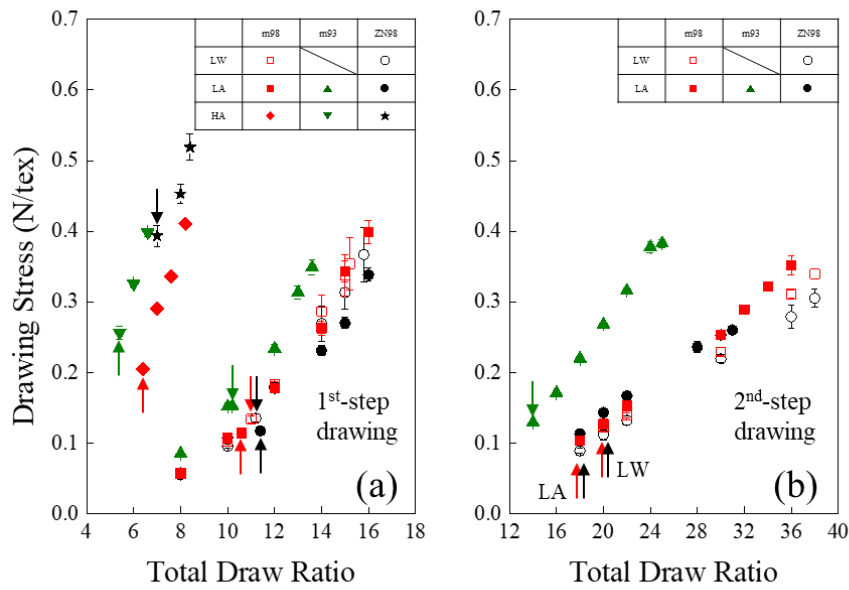


Fig. 2.4 Drawing stress of 1st (a) and 2nd (b) step drawing plotted against the total draw ratio. Markers indicating polymer type and spinning conditions are defined in the figure. The whitening draw ratio for each condition is indicated by an arrow.

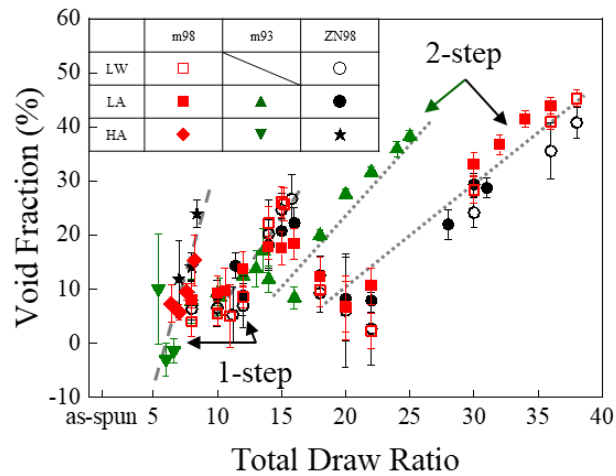


Fig. 2.5 Void fraction plotted against the total draw ratio. Markers indicating polymers type and spinning conditions are listed in the figure.

Table 2.3 Fiber diameters and structural parameters.

Polymer	Spinning Conditions	Total Draw Ratio	Fiber Diameter (D_{obs}) (μm)	Crystalline Dispersion Temperature ($^{\circ}\text{C}$)	T_m ($^{\circ}\text{C}$)	ΔH_m (J/g)	X_{DSC} (%)	X_{WAXD} (%)
m98	LW	1 (as-spun)	185	-	165	89	42	-
		10	60	101	-	-	-	53
		15	55	116	-	-	-	53
		18	46	120	168	116	56	66
		30	40	134	171	128	61	73
		38	40	140	170	137	65	73
	LA	1 (as-spun)	182	-	167	84	40	-
		10	61	106	-	-	-	57
		12	57	110	-	-	-	58
		14	54	114	-	-	-	56
		15	52	117	-	-	-	57
		18	46	122	169	148	71	64
		30	41	134	171	139	67	69
	36	41	139	172	134	64	71	
	HA	1 (as-spun)	66	-	166	93	44	-
m93	LA	1 (as-spun)	185	-	150	65	31	-
		10	61	106	-	-	-	52
		13	55	116	-	-	-	52
		14	52	120	142	110	52	60
		18	49	127	150	101	49	62
		22	48	137	150	104	50	64
		25	47	146	152	122	58	67
	HA	1 (as-spun)	67	-	148	71	34	-
	ZN98	LW	1 (as-spun)	185	-	165	78	38
10			60	102	-	-	-	52
15			55	114	-	-	-	54
18			46	120	167	114	55	66
30			39	133	170	132	63	71
38			39	139	171	121	58	74
LA		1 (as-spun)	184	-	166	89	43	-
		10	61	104	-	-	-	55
		12	56	108	-	-	-	56
		14	54	115	-	-	-	57
		15	53	112	-	-	-	56
		18	46	124	168	132	63	70
		30	40	134	170	144	69	73
HA		1 (as-spun)	67	-	166	95	45	-

The 15–20 K lower drawing temperature of low stereoregularity iPP (m93) than high stereoregularity iPP (m98) should be caused by the lower melting temperature, as shown in **Table 2.1**. The lower molecular mobility of the lower drawing temperature likely caused a lower whitening draw ratio, lower maximum draw ratio, greater whitening drawing stress, and larger void fraction of the low stereoregularity iPP (m93) fibers compared with those features of the high stereoregularity iPP (m98) fibers. The 2nd-step drawing at a temperature higher than the melting temperatures of the raw polymer is noteworthy. The high drawing temperature can be explained by the large drawing stress of the 2nd-step drawing applied to the already drawn fibers which have a high molecular orientation [9]. A greater drawing stress for the narrower molecular weight distribution iPP film is explained by the cooperative and homogeneous deformation of the whole lamellae structure [10]. Similarly, the greater drawing stress of metallocene catalyst-synthesized iPP (m98) fibers observed in this study might be explained by the homogeneous deformation of the molecular chain networks.

3.3 Tensile Properties

The tensile strength and initial modulus of fibers are shown in **Fig. 2.6**. Whereas the initial modulus increased monotonically with the draw ratio, the tensile strength had a maximum value around the whitening draw ratio for all conditions. High stereoregularity metallocene catalyst-synthesized iPP (m98) attained the highest maximum tensile strength and maximum initial modulus fibers among the three polymer types. That is, the fibers having tensile strength of 1.36 N/tex (~1.2 GPa) and initial modulus of 27.4 N/tex (~25 GPa) were fabricated by water-quench spinning and two-step drawing of m98. The theoretical maximum tensile strength and initial modulus were respectively 18 GPa [11] and 39–43 GPa [12]. The tensile strength of 1.56 GPa and initial modulus of 40.4 GPa [13] for the ultra-drawn dried gel films of ultra-high molecular weight iPP are the maximum reported values. There have been some reports that a higher tensile strength and initial modulus fibers can be obtained through the use of iPP of a narrower molecular weight distribution, that is Mw/Mn of 3 rather than 5 [14], 3.44 rather than 4.9 [15], and 2.0 rather than 4.7 [16]. The last case compares iPP fibers synthesized by metallocene and Ziegler–Natta catalysts. The higher strength fiber was obtained by the metallocene catalyst iPP although the IPF of 93% was clearly lower than that of the Ziegler–Natta catalyst iPP of 98%. Conversely, the maximum tensile strength obtained in this study is clearly higher than those of 93% IPF metallocene catalyst-synthesized iPP fiber of 10.7 cN/dtex (~0.96 GPa) [16] and 98% IPF metallocene catalyst iPP of 3.5 cN/dtex (~310 MPa) [17]. The maximum strength obtained in this study corresponds to 7% of the theoretical strength, and 90% of the maximum reported value for the ultra-drawn dried gel film. Moreover, the maximum initial modulus obtained in this study corresponds to 60% of the theoretical modulus and is also higher than the maximum reported modulus for the 93% IPF metallocene catalyst-synthesized iPP of 85 cN/dtex (~7.7 GPa) [16]. Therefore, a high stereoregularity, equivalent to that of Ziegler–Natta catalyst-synthesized iPP, is required to fabricate

high-strength and high-modulus metallocene catalyst-synthesized iPP fibers. Even higher values than those reported for m98 might be obtained at the attainable maximum drawing through optimization of melt-spinning and drawing conditions.

The decrease of tensile strength over the whitening draw ratio irrespective of the monotonical increase of initial modulus indicates a depressive effect of whitening on tensile strength. Strength depression by whitening has also been reported for polyvinyl alcohol drawn fibers and has been explained by macroscale void defects formed during drawing [18]. However, the higher attainable tensile strength of m98 fibers in this study cannot be explained simply by the whitening because the whitening draw ratios for m98 and ZN98 were almost the same. **Fig. 2.7** shows SEM images taken in the vicinity of the breaking point after tensile testing of the fibers having almost the maximum tensile strength. Fibrillation at the breaking point was observed only for the Ziegler–Natta catalyst-synthesized iPP (ZN98) fiber of total draw ratio 20.0 but was observed for both fibers of total draw ratio 22.0. Because the whitening draw ratio and the maximum draw ratio were almost the same, differences in the fibrillation process should progress during the tensile testing by coalescence of voids aligned along the fiber axis, contributing to the difference in breaking phenomena. That is, the higher maximum strength of the metallocene catalyst-synthesized iPP (m98) fiber is attributed to fibrillation suppression during the tensile testing. This estimation is supported by the smaller decrease in tensile strength of the metallocene catalyst-synthesized iPP (m98) fiber than that of Ziegler–Natta catalyst-synthesized iPP (ZN98) fiber observed over the whitening draw ratio.

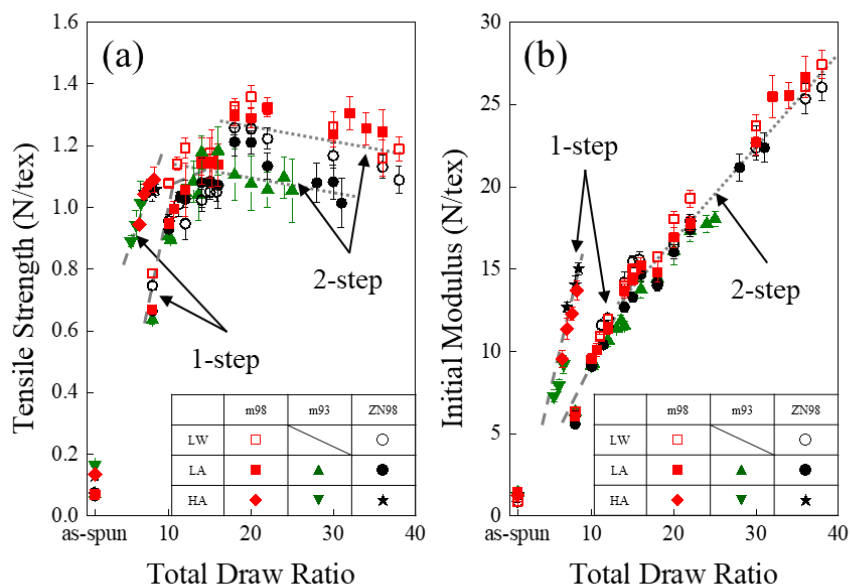


Fig. 2.6 Tensile strength (a) and initial modulus (b) of as-spun, one-step drawn and two-step drawn fibers plotted against the total draw ratio. Markers indicating polymer type and spinning conditions are listed in the figure.

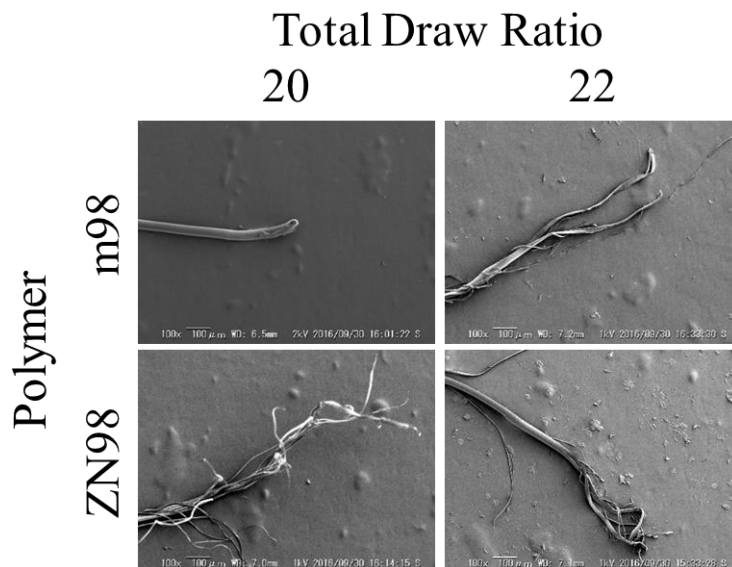


Fig. 2.7 Scanning electron microscope (SEM) image in the vicinity of the breaking point after the tensile tests. Polymers (m98 and ZN98) and total draw ratios (20, 22) are shown in the Figure.

3.4 Creep at 125 °C

Fig. 2.8 shows the creep strain results. Most samples shrink a little before the temperature reached the settled value. Comparing the fibers that had almost the maximum strength for both one- and two-step drawn fibers, the Ziegler–Natta catalyst-synthesized iPP (ZN98) fibers had the greatest creep strain, whereas no clear differences were observed in the creep strains of metallocene catalyst-synthesized iPP (m98 and m93) fibers. These results indicate that the width of the molecular weight distribution affects the high-temperature creep behavior of the drawn fibers. The crystal restructuring under the applied stress might explain the difference in creep behavior because 125 °C exceeds the reported crystalline dispersion temperature [19]. Therefore, the difference in the crystalline state of the drawn fibers is analyzed in the following sessions (3.5–3.7).

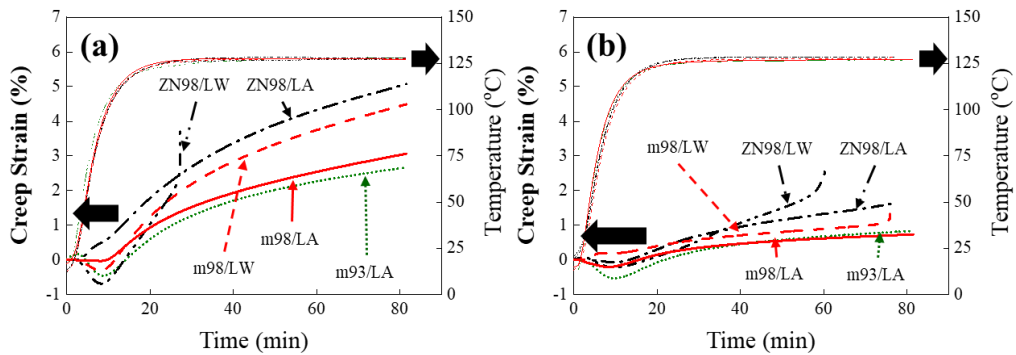


Fig. 2.8 Creep behavior measured for one-step (a) and two-step (b) drawn fibers. Total draw ratios were (a) 15 (m98, ZN98), 13 (m93), and (b) 18. Polymer type and spinning conditions of each sample are noted in the figure. Temperatures of each measurement are also shown by the thin line.

3.5 Viscoelastic properties

Table 2.3 shows the crystalline dispersion temperature obtained from the loss tangent ($\tan \delta$) peak. The crystalline dispersion temperature increased with the draw ratio, whereas no clear differences in the polymer were observed at the same draw ratios. The iPP crystalline dispersion was identified by the c-shear relaxation process, that is, a c-slip process [20]. Increases of the crystalline dispersion temperature with increasing draw ratio have been previously reported [19], and explained by an increase in crystallinity and amorphous orientation. However, the difference in creep behavior shown in **Fig. 2.8** cannot be explained by the crystalline dispersion temperature.

3.6 DSC analysis

The melting temperature, heat of fusion, and X_{DSC} values determined from the curve are listed in **Table 2.3**. The low stereoregularity iPP (m93) fibers clearly had the lowest melting temperature and crystallinity. All the melting temperatures increased with draw ratio whereas the heat of fusion (crystallinity) did not change. The increases in melting temperature and crystalline dispersion temperature are attributed to the increase of crystallinity and amorphous orientation. The increase of crystallinity and amorphous orientation decrease the chain mobility (entropy) of the amorphous region [9], and increase the initial modulus of the fiber, as shown in Section 3.3.

Melting temperature and crystallinity decrease with the decrease of stereoregularity [21-23]. In particular, regio-defects decrease the melting temperature [21]. Because regio-defects tend to be formed by metallocene catalysts, the metallocene catalyst-synthesized iPP has a lower melting temperature than that of the Ziegler-Natta catalyst-synthesized iPP, even in the case that the polymers have the same IPF [5, 21, 24-26]. However, the m98 used in this study has the same melting temperature as that of ZN98, as shown in **Table 2.1**, because it not only has the same IPF but also has fewer regio-defects.

3.7 X-ray analyses

The crystallinity index and crystallite size of the drawn fibers were estimated from the WAXD images. For this purpose, the diffraction angle profile was separated into α -crystal peaks and an amorphous halo. Before the separation, the intensity profiles were integrated along the inclination angle to cancel the orientation effect, and a Lorentz correction was used. The obtained profile of $10^\circ < 2\theta < 23^\circ$ was separated into five α -crystal diffraction features assigned to (110), (040), (130), (111), and (-131), and an asymmetric amorphous halo. However, the mesophase was not considered because a diffraction peak at $2\theta = 15^\circ$ was not observed for all drawn fibers. The profile of each diffraction peak was assumed to be Pearson VII type, as defined in Eq. 2.4, where I_0 , Φ_p , τ , and $m = 2.5$ are the intensity, position, half-width, and shape parameters of each diffraction peak, respectively. For the asymmetric amorphous halo [27], the peak position and low- and high-side peak widths were fixed at

$2\theta = 17^\circ$ [28], 5.8° , and 19° , respectively. **Fig. 2.9** shows an example of an integrated intensity profile and its fitting curve. The fitting curve agreed well with the experimental data. Through the use of the integrated intensity and peak width obtained from the peak separation, the crystallinity index (X_{WAXD}) and crystallite size of (110) diffraction feature (L_{110}) were determined by Eq. 2.5 and the Scherrer's equation (Eq. 2.6), respectively. The I_c and I_a in Eq. 2.5 are the integrated intensities of five α -crystal diffraction features and the amorphous halo, and the constant K and X-ray wavelength λ in Eq. 2.6 were 0.918 and 0.154 nm, respectively. The peak width β was determined by $\beta^2 = \tau^2 - \beta_I^2$, where $\beta_I = 0.1^\circ$ is the contribution to the width from the measuring device.

$$I(\phi) = \frac{I_0}{\left\{1 + 4\left(\frac{\phi - \phi_p}{\tau}\right)^2 \left(\frac{1}{2m-1}\right)\right\}^m} \quad (2.4)$$

$$X_{WAXD} = \frac{I_c}{I_c + I_a} \quad (2.5)$$

$$L_{hkl} = \left(\frac{K\lambda}{\beta \cos(\phi_p/2)} \right) \quad (2.6)$$

The obtained crystallinity indexes and crystallite sizes are shown in **Table 2.3** and **Fig. 2.10**. For both these features, the two-step drawn fibers had higher values than those of the one-step drawn fibers. The low stereoregularity iPP (m93) fibers also had lower values than those of the high stereoregularity iPP (m98 and ZN98) fibers at the same draw ratio. The latter tendency is consistent with the melting temperature and crystallinity, as shown in Section 3.6. Therefore, the low crystallinity index and crystallite size of low stereoregularity iPP were probably caused by the low drawing temperature, which was induced by the low stereoregularity of the polymer. The low drawing temperature—which also led to the low maximum draw ratio, as shown in Section 3.2—probably resulted in the low maximum tensile strength and initial modulus, as shown in Section 3.3.

On the other hand, if the IPF was the same, the polymerization catalyst type and molecular weight distribution had no effect on the crystallinity and crystallite size of the drawn fiber. The crystallite size of the one-step drawn fiber decreased with draw ratio, but saturated for total draw ratio 12, the whitening draw ratio, as shown before. Sakurai et al. explained that the crystallite size decreases with the draw ratio in batch drawn iPP films by fragmentation of the lamellar structure formed along the drawing direction [10]. According to this explanation, the saturation indicates the termination of lamellar crystal fragmentation at the draw ratio. Over the draw ratio, the drawing stress starts to concentrate on the inter-fibrillar tie-chain. Owing to breakage of inter-fibrillar tie chain, macroscale voids were developed with slippage between fibrils.

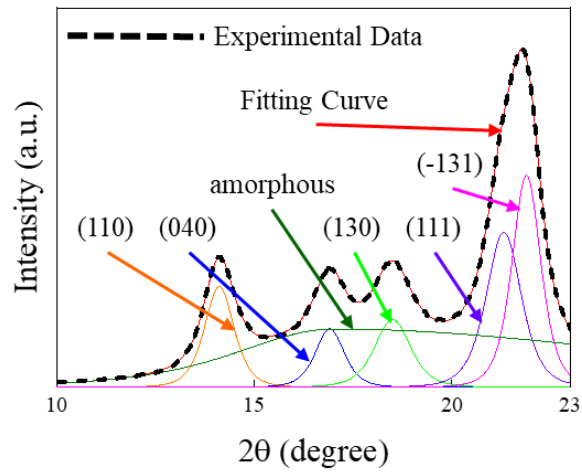


Fig. 2.9 Intensity profile of m98/LA fiber one-step drawn to be 16 times. The profile along the diffraction angle was averaged over the inclination angle, and a Lorentz correction was applied. Fitting curve and profiles for each diffraction feature are also shown.

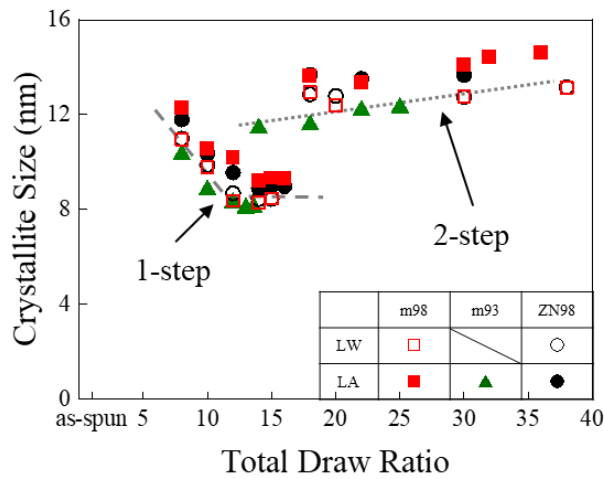


Fig. 2.10 Crystallite size determined from (110) diffraction feature plotted against the total draw ratio. Polymer type and spinning conditions are listed in the figure.

An example of small angle X-ray scattering (SAXS) image of the drawn fiber is shown in **Fig. 2.11 (a)**. There was no meridian long-period peak but an equatorial streak was observed. The equatorial streak originated from the fibrillar structures, i.e., microfibrils and nano-sized voids. To evaluate the amount, the intensity profile of $0.039 \text{ nm}^{-1} < q < 0.427 \text{ nm}^{-1}$ was integrated after Lorentz correction [**Fig. 2.11(b)**]. In addition, the correlation length (ξ) of the structure was determined by a Debye plot of Eq. 2.7 [**Fig. 2.11(c)**], which showed a linear relationship in the range of $0.1 \text{ nm}^{-2} < q^2 < 0.18 \text{ nm}^{-2}$ for all samples.

$$\sqrt{\frac{I_0}{I(q)}} = 1 + \xi^2 q^2 \quad (2.7)$$

The obtained integrated intensities and correlation lengths are shown in **Fig. 12** and **Fig. 13**. Both values began to increase over the whitening draw ratio. The increases of one-step drawn fibers were steeper than those of two-step drawn fibers. The integrated intensity for the same ratio drawn fiber increased in the order: ZN98 < m98 < m93. The obtained correlation length did not exceed 30 nm, which is much shorter than the wavelength of visible light; hence, the structures evaluated by the integrated intensity could not be considered to be macroscale voids causing fiber whitening [18] but were rather 10 nm-sized nanoscale voids.

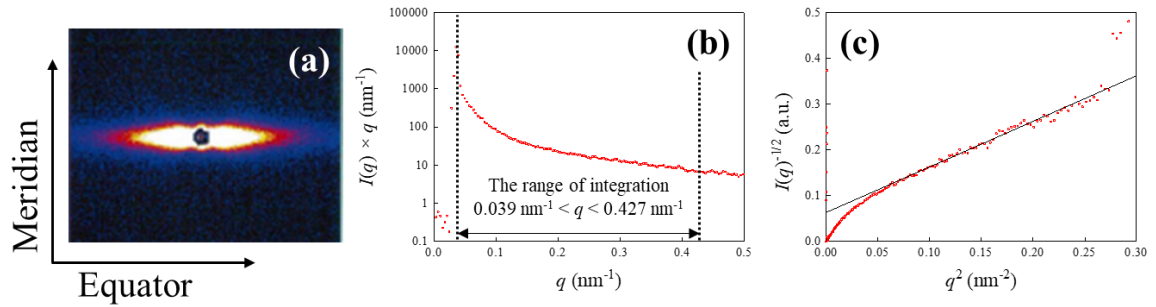


Fig. 2.11 Small angle X-ray scattering pattern of m98 fiber one-step drawn to be 12 times (a). The $q-I(q)q$ (b) and $q^2 - I(q)^{-1/2}$ (c) plots of the equatorial streak used to estimate the amount and correlation length of nanoscale void are also shown.

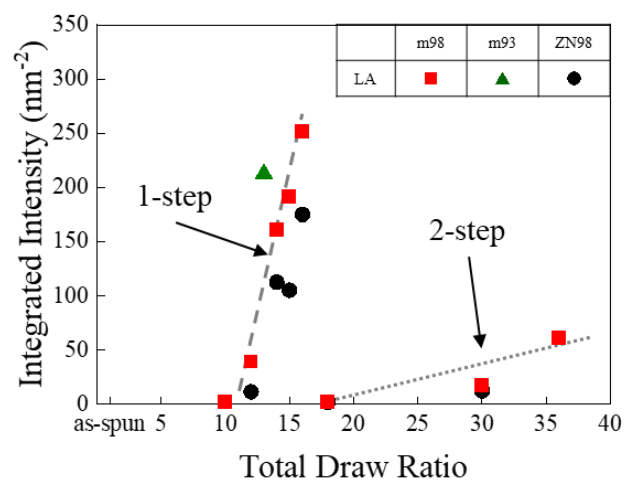


Fig. 2.12 Integrated intensity of SAXS equatorial streak plotted against the total draw ratio. Polymer type and spinning conditions are listed in the figure.

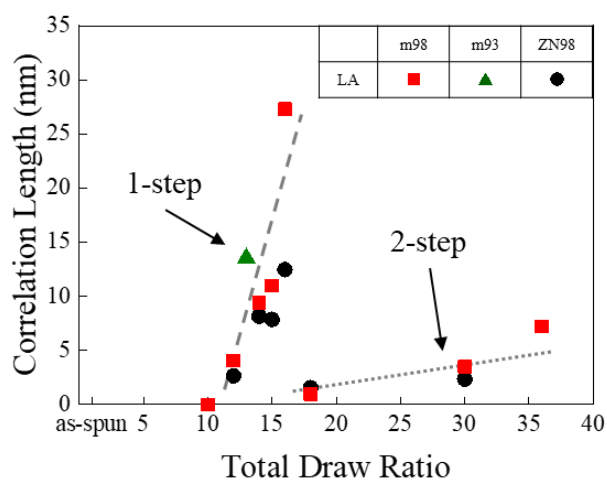


Fig. 2.13 Correlation length plotted against the total draw ratio. Polymer type and spinning conditions are listed in the figure.

3.8 Effects of molecular weight distribution

The integrated intensity determined from the SAXS results is plotted against the void fraction (**Fig. 2.14**). An almost linear relationship was observed between these factors for all samples. However, the two-step drawn fibers had a higher void fraction than that of one-step drawn fibers at the same integrated intensity. The higher void fraction of the two-step drawn fibers is likely caused by drawing of drawn fiber in which the fibril structure is already formed, whereas the low-orientation fiber was drawn in the 1st-step drawing. The higher drawing temperature of the 2nd-step drawing suppressed nanoscale void formation, whereas the greater drawing stress concentration of the inter-fibrillar tie-chain promoted macroscale void development. **Fig. 2.14** also shows that more macroscale voids tended to form in the Ziegler-Natta catalyst-synthesized iPP (ZN98) fiber than in the metallocene catalyst-synthesized iPP (m98) fiber having an equivalent amount of nanoscale voids. The growth of macroscale voids from nanoscale voids was suppressed for the m98 fiber drawn to the higher draw ratio, likely because uniform-sized fibrils were formed by drawing of the uniform molecular chain network formed in the melt-spinning process of the narrower molecular weight distribution iPP.

A fibril structure model is shown in **Fig. 2.15** to explain this hypothesis. As shown in Section 3.1, the molecular orientation of the metallocene catalyst-synthesized iPP (m98) as-spun fiber was higher than that of the Ziegler-Natta catalyst-synthesized iPP (ZN98), irrespective of the use of the same raw polymer, MFR, and spinning conditions. Conversely, the spherulite-like structure formed in the Ziegler-Natta catalyst-synthesized iPP as-spun fiber indicates a higher temperature solidification in the spinning line. These results can be explained by the more uniform molecular chain network of molten metallocene catalyst-synthesized iPP bearing the spin-line stress more uniformly. The as-spun fibers having a uniform molecular chain network also bear the drawing stress uniformly and a uniform fibril structure should be formed in the drawn fiber. The uniform drawing stress applied to the inter-fibrillar tie-chain should suppress the breakage of the tie-chains and the development of macroscale voids. This model agrees with a report by Sakurai et al. [10] that more homogeneous deformation during drawing is caused by the narrower molecular weight distribution iPP. The model is also consistent with the model of Lu et al. [29, 30] that the macroscale void formation and whitening are caused by breakage of load-bearing inter-fibril / micro-fibril tie chains. In addition, our model is supported by reports for polyethylene terephthalate fibers that fibers of higher tensile strength are obtained by drawing as-spun fibers with a uniform molecular chain network [31, 32]. A higher attainable maximum tensile strength was also obtained for high stereoregularity metallocene catalyst-synthesized iPP in this study (**Fig. 2.6**). This increase in tensile strength is explained by fibrillation suppression (**Fig. 2.7**) of the uniform molecular chain network. That is, a higher maximum tensile strength should be attained owing to a less pronounced decrease in tensile strength at higher draw ratio, through fibrillation suppression, despite the increase of drawing stress with draw ratio (**Fig. 2.4**). The lower creep at high temperatures (**Fig. 2.8**) can be also explained by the uniform fibril structures

bearing the external force evenly.

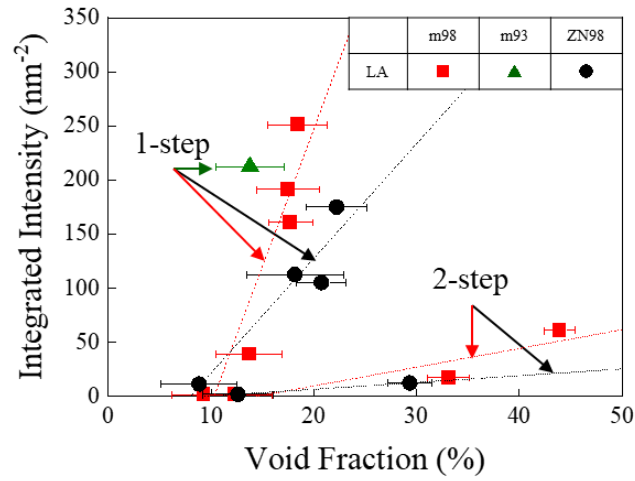


Fig. 2.14 Integrated intensity of SAXS equatorial streak plotted against void fraction, which was estimated from the fiber diameter.

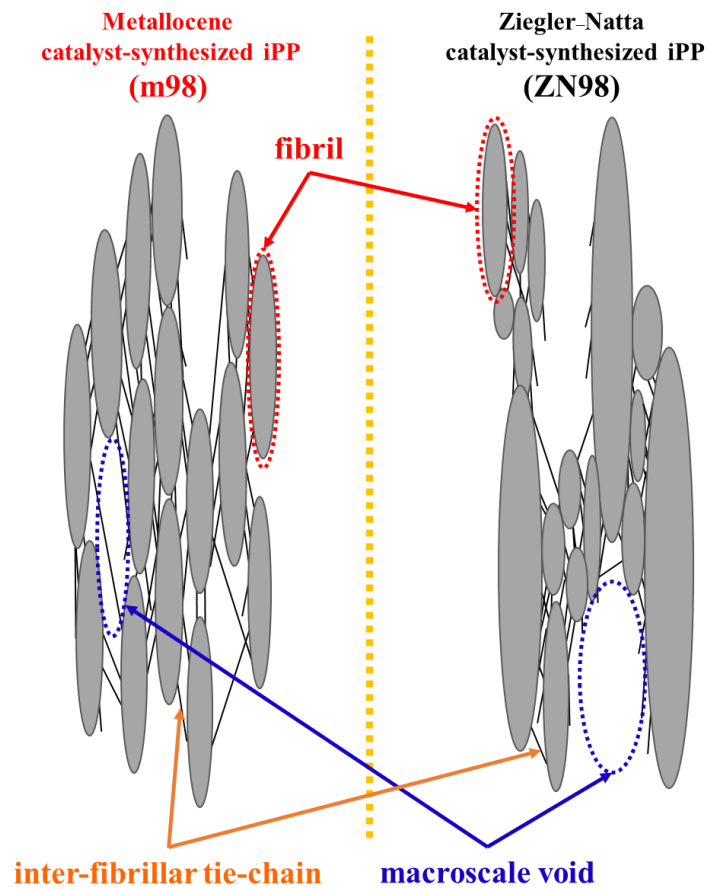


Fig. 2.15 Model of the fibril structure in the drawn fiber of each polymer.

4 Conclusion

The effects of iPP stereoregularity and molecular weight distribution on the properties and structure of fibers were investigated for metallocene catalyst-synthesized iPP with an IPF of 98% and Mw/Mn 2.5 (m98), metallocene catalyst-synthesized iPP with an IPF of 93% and Mw/Mn 2.5 (m93), and a Ziegler–Natta catalyst-synthesized iPP with an IPF of 98% and Mw/Mn 3.5 (ZN98). The fibers were obtained by melt spinning, and drawn twice. To compare the attainable maximum tensile strength, each polymer fiber was taken-up at the minimum stable MDR, and the as-spun fibers were drawn to the maximum draw ratio at the drawable maximum temperature for each polymer.

The high stereoregularity metallocene catalyst-synthesized iPP (m98) clearly contributed to greater tensile strength and initial modulus. These results are explained by the greater maximum draw ratio, crystallinity, and crystallite size. These factors are all related to the higher drawing temperature that is achievable because of the higher melting temperature. As a result, the maximum tensile strength of 1.36 N/tex (~1.2 GPa) and a maximum initial modulus of 27.4 N/tex (~25 GPa) were obtained for m98 fiber drawn over 20 times. The high stereoregularity metallocene catalyst-synthesized iPP fibers also indicated a higher birefringence and a greater drawing stress than those of the Ziegler–Natta catalyst-synthesized iPP (ZN98) fiber at the same draw ratio. Moreover, the metallocene catalyst-synthesized iPP (m98) fiber having almost the same tensile strength of Ziegler–Natta catalyst-synthesized iPP (ZN98) fibers also had a lower creep strain at 125 °C under 50-MPa tensile stress. There was almost no difference in the crystalline dispersion temperature, melting temperature, crystallinity, and crystallite size observed between the drawn fibers of different catalyst iPP spun and drawn under the same conditions; however, the tensile strength of the m98 drawn fiber decreased less for a total draw ratio greater than 14 than did the ZN98 fiber, which contributed to a higher attainable maximum tensile strength of the m98 fiber. The fibrillation at fracture and whitening were also suppressed for metallocene catalyst-synthesized iPP (m98). Furthermore, macroscale void formation, estimated by the fiber diameter, in the Ziegler–Natta catalyst-synthesized iPP (ZN98) fiber was more pronounced than that in the metallocene catalyst-synthesized iPP (m98) fiber having an equivalent amount of nanoscale voids (~10 nm) estimated from the equatorial streak of the SAXS. The lower content of macroscale voids form in the drawing of the m98 fibers was consistent with the suppressed fibrillation tendency at fracture. These tendencies can be explained by the more uniform molecular chain network which should be brought by the narrower molecular weight distribution of metallocene catalyst-synthesized iPP. The higher attainable tensile strength and lower creep strain at high temperature are also explained by the uniform molecular chain network.

References

- [1] K. Koike, Y. Ohkoshi, K.H. Kim, T. Ikaga, K. Toyoda, T. Kunimitsu, Japan Patent, Prime Polymer Co. Ltd., Shinshu Univ., Mitsui Chemicals Inc., 2017, WO2017/209283.
- [2] J. Brandrup, E.H. Immergut, E.A. Grulke, Polymer Handbook 4th edition, A John Wiley and Sons, 1999, pp. VI/11. ISBN 0-471-481718-8.
- [3] J. Brandrup, E.H. Immergut, Polymer Handbook, 2nd edition, John Wiley and Sons, 1975, pp. V-24. ISBN 0-471-09804-3.
- [4] G. Natta, P. Corradini, *Nuovo Cim.* 15 (1960) 40–51. doi:10.1007/BF02731859.
- [5] E.B. Bond, J.E. Spruiell, *J. Appl. Polym. Sci.* 82 (2001) 3223–3236. doi:10.1002/app.2181.
- [6] S. Misra, F.-M. Lu, J.E. Spruiell, G.C. Richeson, *J. Appl. Polym. Sci.* 56 (1995) 1761–1779. doi:10.1002/app.1995.070561307.
- [7] Y.A. Kang, X. Zhao, Y. Ohkoshi, K.H. Kim, *Polym. Eng. Sci.* 56 (2016) 609–616. doi:10.1002/pen.24245.
- [8] Y.A. Kang, Y. Ohkoshi, K.H. Kim, *Polym. -Plast. Technol. Eng.* 55 (2016) 553–558. doi:10.1080/03602559.2015.1093141.
- [9] M. Tosaka, *J. Fiber Sci. Technol.* 74 (2018) P30–P34. doi:10.2115/fiber.74.P-30.
- [10] T. Sakurai, Y. Nozue, T. Kasahara, K. Mizunuma, N. Yamaguchi, K. Tashiro, Y. Amemiya, *Polymer.* 46 (2005) 8846–8858. doi:10.1016/j.polymer.2005.01.106.
- [11] T. Ohta, *Polym. Eng. Sci.* 23 (1983) 697–703 doi.org/10.1002/pen.760231302.
- [12] C. Sawatari, M. Matsuo, *Macromolecules.* 19 (1986) 2653–2656. doi:10.1021/ma00164a036.
- [13] M. Matsuo, C. Sawatari, T. Nakano, *Polym. J.* 18 (1986) 759–774. doi:10.1295/polymj.18.759.
- [14] E. Andreassen, O.J. Myhre, E.L. Hinrichsen, K. Grøstad, *J. Appl. Polym. Sci.* 52 (1994) 1505–1517. doi:10.1002/app.1994.070521015.
- [15] Z.T. Mazraeh-Shahi, M.R.M. Mojtahedi, *J. Text. Inst.* 101 (2010) 547–555. doi:10.1080/00405000802597600.
- [16] S. Ota, Japan Patent, UbeNitro Kasei Co. Ltd., 2001, P2001-123322A.
- [17] R. Xu, P. Zhang, H. Wang, X. Chen, J. Xiong, J. Su, P. Chen, Z. Zhang, *Polymers.* 11 (2019) 1–17. doi:10.3390/polym11040729.
- [18] H. Kawakami, H. Sato, A. Miyoshi, I. Sakai, *Sen'i Gakkaishi.* 29 (1973) T436–T441. doi:10.2115/fiber.29.10_T436.
- [19] A.J. Uddin, Y. Mashima, Y. Ohkoshi, Y. Gotoh, M. Nagura, A. Sakamoto, R. Kuroda, *J. Polym. Sci. Part B Polym. Phys.* 44 (2006) 398–408. doi:10.1002/polb.20681.

- [20] A. Suzuki, T. Sugimura, T. Kunugi, *J Appl Polym Sci.* 81 (2001) 600–608. doi:10.1002/app.1475.
- [21] T. Tsutsui, N. Ishimaru, A. Mizuno, A. Toyota, N. Kashiwa, *Polymer* 30 (1989) 1350–1356. doi:10.1016/0032-3861(89)90059-1.
- [22] C. De Rosa, F. Auriemma, G. De Lucia, L. Resconi, *Polymer.* 46 (2005) 9461–9475. doi:10.1016/j.polymer.2005.07.028.
- [23] T. Takeda, Y. Minami, T. Kanai, *Seikei-Kakou.* 21 (2009) 202–207. doi:10.4325/seikeikakou.21.202.
- [24] E.B. Bond, J.E. Spruiell, J.S. Lin, *J. Polym. Sci. B Polym. Phys.* 37 (1999) 3050–3064. doi:10.1002/(SICI)1099-0488(19991101)37:21<3050::AID-POLB14>3.0.CO;2-L.
- [25] E.B. Bond, J.E. Spruiell, *J. Appl. Polym. Sci.* 82 (2001) 3237–3247. doi:10.1002/app.2182.
- [26] J.M. Gómez-Elvira, P. Tiemblo, M. Elvira, L. Matisova-Rychla, J. Rychly, *Polym. Degrad. Stab.* 85 (2004) 873–882. doi:10.1016/j.polymdegradstab.2004.04.003.
- [27] G. Colombe, S. Gree, O. Lhost, M. Dupire, M. Rosenthal, D.A. Ivanov, *Polymer.* 52 (2011) 5630–5643. doi:10.1016/j.polymer.2011.09.035.
- [28] T. Konishi, K. Nishida, T. Kanaya, *Macromolecules.* 39 (2006) 8035–8040. doi:10.1021/ma060191b.
- [29] Y. Lu, Y. Wang, R. Chen, J. Zhao, Z. Jiang, Y. Men, *Macromolecules.* 48 (2015) 5799–5806. doi:10.1021/acs.macromol.5b00818.
- [30] Y. Lu, Y. Men, *Macromol. Mater. Eng.* 303 (2018). doi:10.1002/mame.201800203.
- [31] M. Masuda, W. Takarada, T. Kikutani, *Int. Polym. Process. J. Polym. Process. Soc.* 25 (2010) 159–169. doi:10.3139/217.2330.
- [32] R. Tomisawa, S. Oneda, T. Ikaga, K.H. Kim, Y. Ohkoshi, K. Okada, H. Masunaga, T. Kanaya, H. Katsuta, Y. Funatsu, *Polymer.* 164 (2019) 163–173. doi:10.1.

Chapter 3

High strength metallocene catalyst-synthesized
polypropylene fibers with high stereoregularity
and high molecular weight

Chapter 3: High strength metallocene catalyst-synthesized polypropylene fibers with high stereoregularity and high molecular weight

1. Introduction

In this Chapter, fibers fabricated using the above type of metallocene iPP with 4 g/10 min melt index were analyzed, including their tensile properties, creep behavior at high temperature, and fiber structure. The molecular weight decrease during melt-spinning at 270–290 °C was also investigated. To estimate the attainable maximum tensile strength, the extruded polymer was taken up at the lowest possible speed, and the as-spun fiber was drawn up to the maximum draw ratio at the highest possible temperature. The nanometer to micrometer scale fiber structures were analyzed by wide, small, and ultra-small angle X-ray measurements. The obtained results were compared with those of Ziegler–Natta iPP with equivalent molecular weight and stereoregularity. They were also compared with the results of 20 g/10 min melt index samples [1].

2. Experimental

2.1 Polymer

Three types of iPP polymer samples were investigated in this study: metallocene catalyst-synthesized iPP with 4 g/10 min melt index (m4), and Ziegler–Natta catalyst-synthesized iPP with 4 g/10 min melt index (ZN4) and 3 g/10 min melt index (ZN3). ZN4 was obtained from ZN3 by thermal cracking. The results of these iPP samples were compared with the reported values for 20 g/10min melt index samples (m20 and ZN20) in Chapter 2. All of the polymers were supplied by Prime Polymer Co., Ltd. (Tokyo, Japan). The characteristics of each polymer sample are given in **Table 3.1** [1, 2].

Table 3.1 Materials

Polymer	Catalyst	*MI / g/10min	M_w / g/mol	M_n / g/mol	M_w/M_n	**IPF x100%	T_m / °C
ZN3	Ziegler–Natta	3	358,000	70,100	5.1	98	162
m4	metallocene	4	287,000	98,000	2.9	98	162
ZN4	Ziegler–Natta	4	309,000	92,600	3.3	98	162
m20 [1]	metallocene	20	176,000	70,000	2.5	98	162
ZN20 [1]	Ziegler–Natta	20	214,000	61,500	3.5	98	162

*Melt index. **Isotactic pentad fraction.

2.2 Spinning and drawing conditions

The source polymers were melt-extruded with a BT-30-S 2-42-L twin-screw extruder (Research Laboratory of Plastics Technology Co., Ltd., Tokyo, Japan). A spinneret with diameter of 0.7 mm and length of 2.1 mm was used for m4 and ZN4, while a spinneret with diameter of 1.0 mm and length of 3.0 mm was used for ZN3. The spinning conditions are listed in **Table 3.2**. Here, v and W are the take-up speed and mass flow rate, respectively.

The as-spun fibers were continuously drawn by the speed difference between the feed and take-up rollers (first drawing step), and the 10 times drawn fiber was drawn again (second drawing step). The total draw ratio is defined as the product of the draw ratios for the two drawing steps. The feed speed was fixed at 1 m/min, and a hot plate heater with a contact length of 225 mm was used for both drawing steps. The drawing temperature was fixed at the drawable maximum temperature of each fiber. That is, 145 °C for the first drawing step for m4 and ZN4, 150 °C for the first drawing step for ZN3, and 180 °C for all of the second drawing steps. The drawing tension was measured by a tension meter (HS-1500S, Eiko Sokki Co., Ltd., Osaka, Japan) equipped with a 1 N pickup sensor, except for the first drawing step for ZN3 where a 2 N pickup sensor was used. The fiber diameter (D_{obs}) was measured by a diameter detector (LS-9006, Keyence Co., Ltd., Osaka, Japan) and captured at a sampling period of 100 ms by a data logger (NR-2000, Keyence Co., Ltd.). The drawing stress was calculated from the obtained tension and the fiber fineness, which was measured with a denier tester (DENICON DC-21, Search Co., Ltd., Kyoto, Japan), and averaged for every 12 fibers.

Table 3.2 Spinning conditions and properties of the as-spun fibers

Polymer	Spinning Temperature / °C	v / m min ⁻¹	W / g min ⁻¹	D_{obs} / μm	T_m / °C	ΔH_m / kJ/kg	Birefringence	NDR
ZN3	270	75	3.0	233	167	89	0.0040	5.2
	280	150	3.0	166	-	-	-	-
	290	150	3.0	165	-	-	-	-
m4	270	62.5	1.5	182	166	87	0.0036	5.4
	280	125	3.0	182	166	85	0.0030	5.4
	290	125	3.0	181	166	91	0.0018	5.6
ZN4	270	62.5	1.5	180	167	84	0.0026	5.1
	280	125	3.0	181	166	86	0.0006	5.1
	290	150	3.0	165	165	81	0.0003	4.6
m20 [1]	220	125	3.0	182	167	84	0.0017	5.9
ZN20 [1]	220	125	3.0	184	166	89	0.0003	5.2

2.3 Molecular weight

The molecular weight and molecular weight distribution (M_w/M_n) of the polymer pellet before spinning and the as-spun fibers were determined by gel permeation chromatography (Alliance GPC-2000, Waters Co., Massachusetts, USA). TSKgel GNH6-HT and TSKgel GNH6-HTL separation columns were used at 140 °C. To the separation column, 400 μ L of 15 mg/10 mL iPP concentration was injected, and *o*-dichlorobenzene with 0.025 mass % butylated hydroxytoluene antioxidant as the mobile phase was transferred at 1.0 mL/min. A differential refractometer was used for detection, and polystyrene (Tosoh Co., Tokyo, Japan) was used as the reference material.

2.4 Microscopy

The birefringence of the fibers was measured at room temperature using a polarized microscope (BX51-33POC, Olympus Co., Ltd., Tokyo, Japan) with a halogen lamp light source. Tricresyl phosphate was used as the immersion oil. The average and standard deviation of the birefringence were calculated for every 10 samples.

2.5 Tensile test

The tensile test was performed at room temperature using an Autograph AGS-X instrument (Shimadzu Co., Ltd., Kyoto, Japan) equipped with a 50 N load cell and an air chuck. The initial length was 40 mm, and the elongation rate was 100 mm/min for the as-spun fibers and 40 mm/min for the drawn fibers. The strength and initial modulus obtained by the nominal stress–nominal strain curve were averaged for every 12 samples. The initial modulus was calculated for the strain range of 0.13%–1.8%. The fiber fineness was also used for the stress, similar to the drawing stress described in Section 2.2. The fineness of the drawn fibers was measured by the same method, while the fineness of the as-spun fibers was calculated from the fiber diameter assuming an iPP density (ρ) of 0.9 g/cm³ [3]. The fiber diameter was measured by a digital microscope (VHX-1000, Keyence Co., Ltd.).

2.6 Thermomechanical analysis and differential scanning calorimetry

The thermal creep behavior was measured by a thermomechanical analyzer (SS6100 thermal analysis rheology system, SII NanoTechnology Co., Ltd., Tokyo, Japan) at 125 °C. The sample length was 10 mm and the applied stress was 50 MPa. Differential scanning calorimetry (DSC, Thermoplus DSC8230, Rigaku Co., Ltd., Tokyo, Japan) was performed from room temperature to 200 °C at 10

K/min. Approximately 2 mg of cut fiber was enclosed in an aluminum pan. Nitrogen gas was flowed at 50 mL/min during the measurement. The melting peak temperature (T_m) and heat of fusion (ΔH_m), which is defined as the difference between the integrated heat of melting and cold crystallization, were obtained from the DSC curve.

2.7 X-ray measurements

Wide-angle X-ray diffraction (WAXD) and small-angle X-ray scattering (SAXS) images were recorded with RA-Micro7/R-AXIS-IV++ and NanoViewer/PILATUS 100K detector systems (Rigaku Co., Ltd.). The camera length and exposure time for WAXD and SAXS were 250 mm and 10 min, and 1380 mm and 60 min, respectively. The X-ray source for the measurements was Cu-K α generated at a tube voltage of 40 kV and tube currents of 20 and 30 mA. A bundle of one-directional aligned fibers was used for the specimen with 3 mm width and 150 μ m thickness. Ultra-small angle X-ray scattering (USAXS) images were also recorded by a synchrotron X-ray beam (SPring-8 BL19B2) with a PILATUS 2M detector system (DECTRIS Ltd., Baden-Daettwil, Switzerland). The synchrotron X-ray energy was 18 keV, and the beam dimensions were 400 μ m \times 500 μ m along the vertical and horizontal direction. The camera length and exposure time were 40,835 mm and 5 min. A bundle of one-directional aligned fibers was used for the specimen.

3. Result and discussion

3.1 Thermal degradation during the melt spinning process

The number-average molecular weight (M_n), weight-average molecular weight (M_w), and M_w/M_n of the pellets and as-spun fibers are shown in Fig. 3.1. Both the average molecular weights of the as-spun fibers were lower than those of the pellets, particularly for high spinning temperature. Moreover, a greater decrease in the weight-average molecular weight was observed for the Ziegler–Natta catalyst-synthesized iPPs, particularly for ZN3. This tendency was also observed for the low molecular weight samples, but the difference was not as large. A large decrease of the weight-average molecular weight has previously been reported for iPP with a wide molecular weight distribution [4]. The larger decrease of the weight-average molecular weight than that of the number-average molecular weight indicates that the long-chain molecules are more easily broken by thermal decomposition. The smaller decrease in the weight-average molecular weight for the metallocene catalyst-synthesized iPPs can also be explained by their smaller fraction of long-chain molecules.

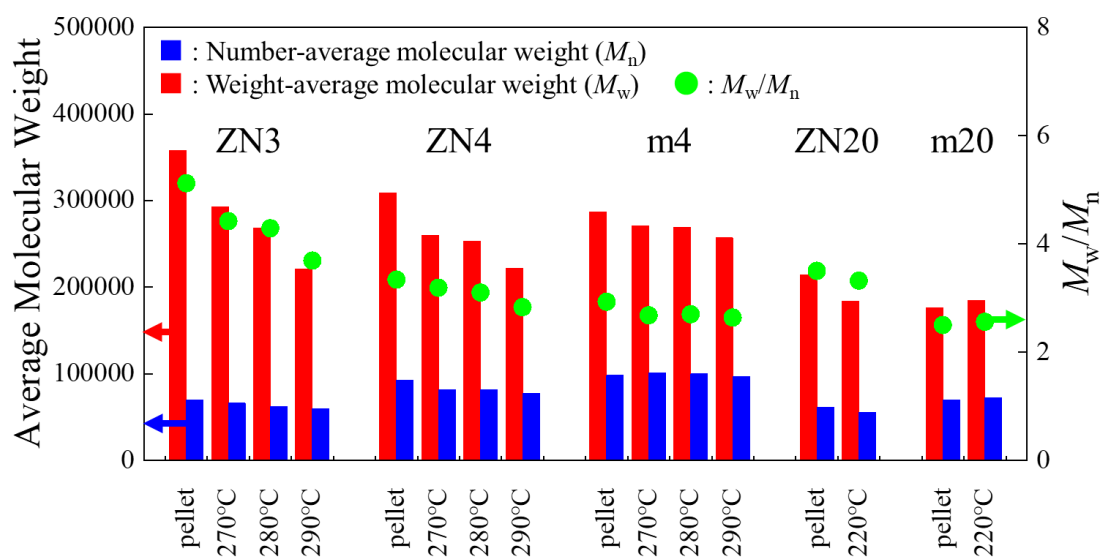


Fig. 3.1 Number-average molecular weight (M_n), weight-average molecular weight (M_w), and M_w/M_n of the pellets and as-spun fibers. The polymer names and spinning temperatures are shown in the figure.

The DSC results for the as-spun fibers, the melting temperature (T_m) and heat of fusion (ΔH_m), are listed in **Table 3.2**. The polymerization catalyst and molecular weight had almost no effect on both T_m and ΔH_m . The equivalent melting temperatures indicate that there were almost no structural defects, so-called regio-defects [5], in the chains of all of the iPP samples synthesized with different catalysts. The different catalysts also caused different chain ends, which can affect the higher-order structure of the obtained fiber, but the effect on the fiber strength can be ignored compared with the effects of the molecular weight and molecular weight distribution. Therefore, in this study, the effects of the molecular weight and its distribution on the structure and properties of the obtained fiber were focused.

All of the as-spun fibers showed α -crystal diffraction features oriented along the a^* axis (**Fig. 3.2**). There was almost no difference in the birefringence between the metallocene and Ziegler–Natta iPPs (**Table 3.2**). A particle-like structure, which is thought to be a spherulite, was observed in the polarization microscope images of all of the fibers (**Fig. 3.3**). Higher crystal orientation, higher birefringence, and a smaller particle-like structure have been reported for m20 as-spun fibers compared with ZN20 fibers, but these tendencies were hardly observed for the high molecular weight fibers. That is, there was a smaller difference of the as-spun fiber structures between the m4 and ZN4 fibers than between the m20 and ZN20 fibers. Because the M_w/M_n differences between the m4 and ZN4 pellet and fibers were also lower than those between m20 and ZN20, in particular, there was only a small difference between the high-temperature-spun m4 and ZN4 fibers, the smaller molecular weight distribution as well as the high molecular weight must be considered to explain the smaller difference.

The m4 fibers had larger natural draw ratio (NDR, **Table 3.2**) than the ZN4 fibers, and the difference was also smaller than for the low molecular weight (m20 and ZN20) fibers. The NDR, which is defined as the ratio of the stretching ratio at which the natural drawing region terminates to the stretching ratio of the upper yield point, corresponds to the maximum extension of the molecular network [6]. Therefore, the NDR is used as an indicator to represent the orientation and homogeneity of a virtual molecular chain network bearing an external force [7, 8]. Larger NDR under the same molecular orientation for the narrower molecular weight distribution (m4) fibers should indicate a more uniformly entangled molecular chain network than for the wider molecular weight distribution (ZN4) fibers. The effect of the molecular weight distribution, that is, the uniformity of the molecular chain network, on the structure and properties of the drawn fiber is discussed in the following Sections.

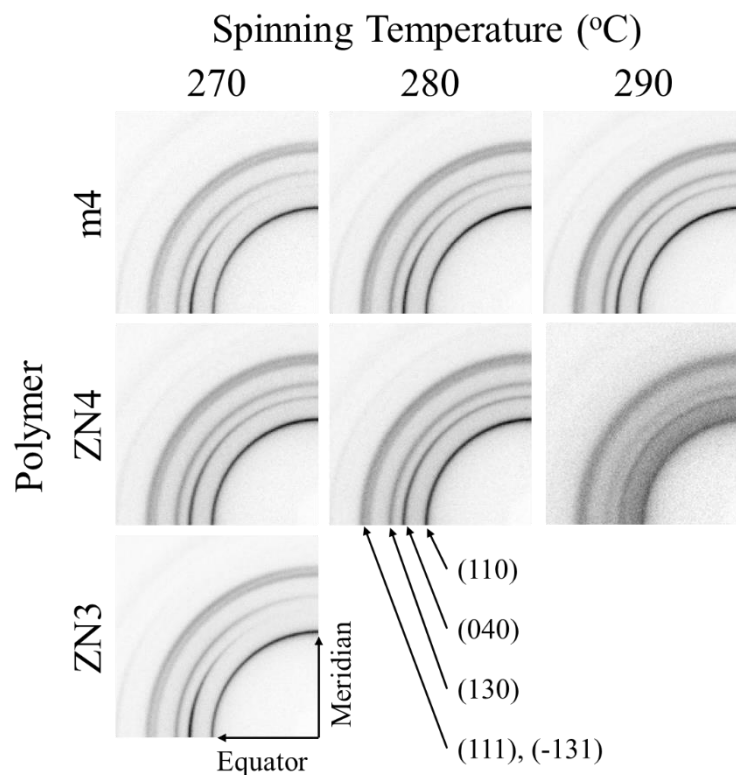


Fig. 3.2 WAXD images of the as-spun fibers. The polymer names (m4, ZN4, and ZN3) and spinning temperatures (270, 280, and 290 °C) are shown in the figure.

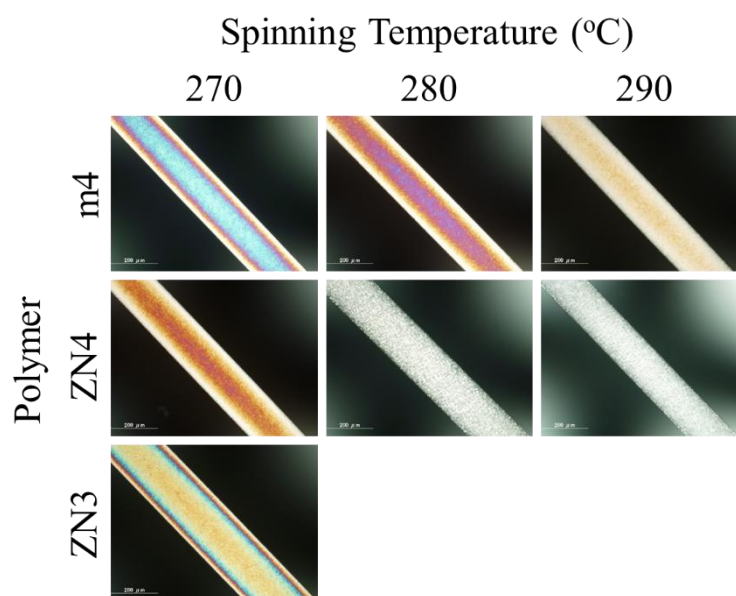


Fig. 3.3 Polarized microscope images of the as-spun fibers. The polymer names (m4, ZN4, and ZN3) and spinning temperatures (270, 280, and 290 °C) are shown in the figure.

3.2 Drawing

The drawing stress for each drawing condition is shown in **Fig. 3.4**. To estimate the attainable maximum fiber strength, each polymer was melt-spun at almost the minimum take-up speed, and maximally drawn at the highest possible drawing temperature. The maximum draw ratio shown in **Fig. 3.4** was determined as the maximum draw ratio where the fiber could be stably drawn for more than 10 min. The fiber whitening draw ratio for each drawing step is also shown in the figure. There were no clear differences between the m4 and ZN4 fibers in terms of their whitening and maximum draw ratios, but they were different than those of the low molecular weight fibers.

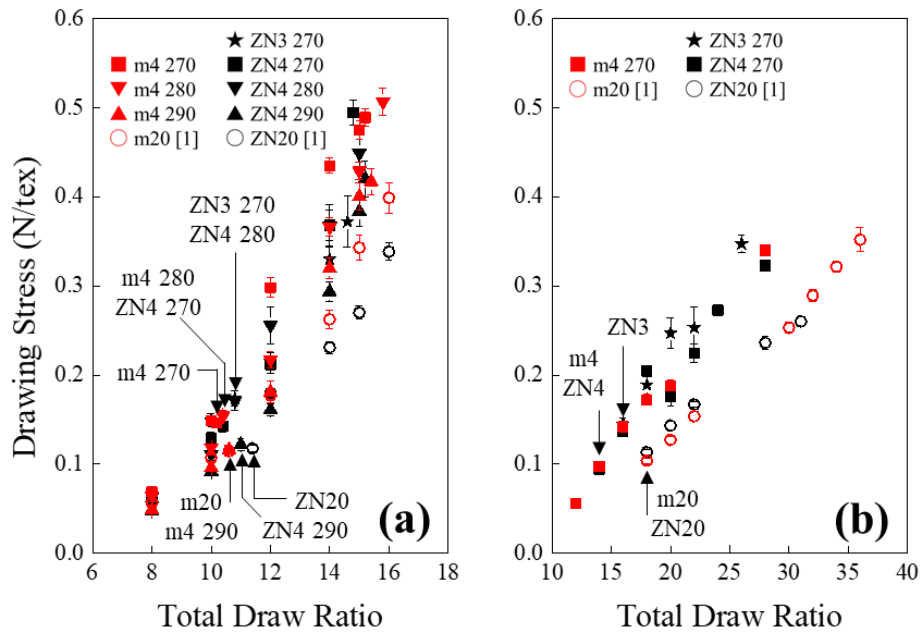


Fig. 3.4 Drawing stress of the (a) first and (b) second drawing steps plotted against the total draw ratio. The symbols indicating the polymers and spinning temperatures are defined in the figure. The whitening draw ratio for each condition is indicated by an arrow.

3.3 Thermo-mechanical properties

The tensile strength and initial modulus of the drawn fibers plotted against the total draw ratio are shown in **Figs. 3.5** and **3.6**, respectively. The tensile strength reached the maximum at around the fiber whitening draw ratio, while the initial modulus monotonically increased with increasing total draw ratio. Higher strength fibers were achieved using m4 than using ZN4, as well as the case using low molecular weight samples. Both the maximum strength and maximum initial modulus of 1.39 N/tex (1.3 GPa) and 26.0 N/tex (23 GPa) were obtained for the m4 fibers fabricated by 270 °C spinning and two-step drawing. The maximum strength of the m4 fibers was higher than that of the m20 fibers, while the maximum modulus was smaller.

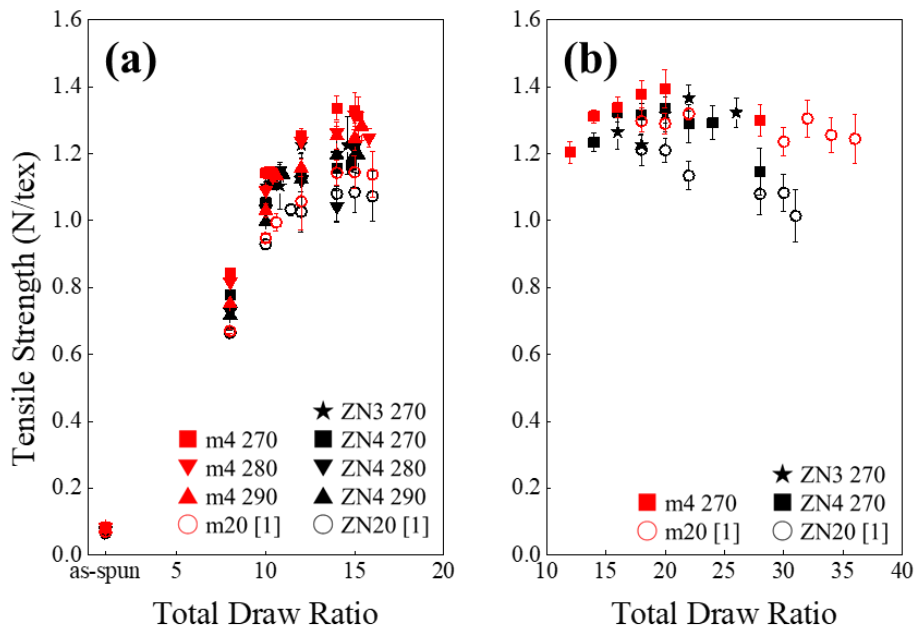


Fig. 3.5 Tensile strength of the (a) as-spun fiber and first drawing step and (b) second drawing step plotted against the total draw ratio. The symbols indicating the polymers and spinning temperatures are defined in the figures.

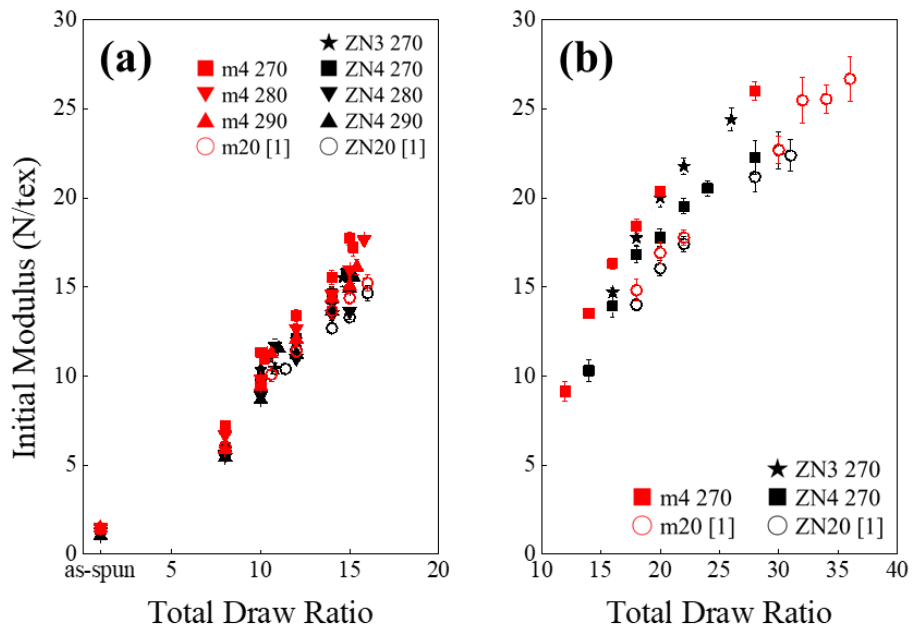


Fig. 3.6 Initial modulus of the (a) as-spun fiber and first drawing step and (b) second drawing step plotted against the total draw ratio. The symbols indicating the polymers and spinning temperatures are defined in the figures.

The creep strain of the fibers, indicating the maximum strength for each polymer and spinning temperature, is shown in **Fig. 3.7**. Most of the fibers slightly shrank before reaching the settled temperature, and the metallocene catalyst-synthesized iPP fibers showed smaller creep strain than the Ziegler–Natta catalyst-synthesized iPP fibers. The metallocene catalyst-synthesized iPP fibers also showed smaller creep strain than the low molecular weight sample. Therefore, the narrower molecular weight distribution restrained fiber creep at 125 °C, even for high molecular weight.

Both 290 °C spun fibers showed a larger creep strain, and they broke below the setting temperature. Yamashita reported from the SAXS measurement on the iPP melt that the correlation length of the density fluctuation began to decrease above 260 °C. The 0.5–0.8-nm-sized density fluctuation, which was presumably a piece of crystallite that was memorized above the melting temperature, is thought to indicate the aggregated structure that may be the crystal nuclei origin. The clear larger creep strain for the 290 °C spun fiber can be explained by the smaller correlation length of the aggregated structure.

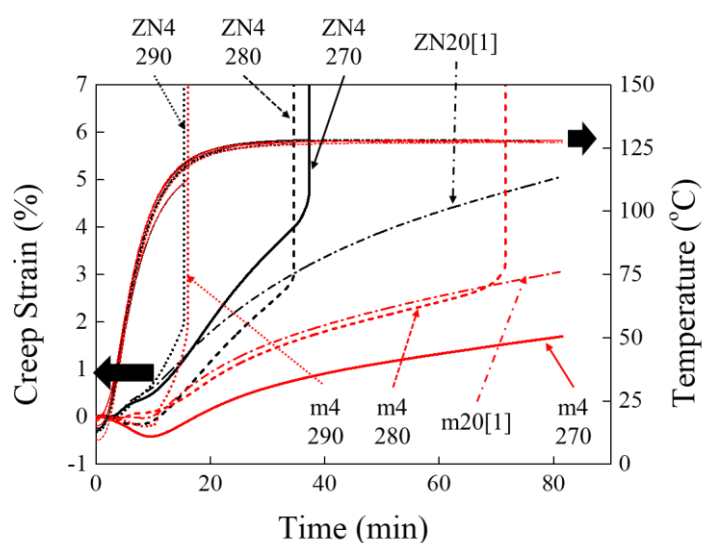


Fig. 3.7 Creep behavior of the one-step drawn fibers. The total draw ratios were 15.0, except for 14.8 for ZN4 270. The polymer and spinning temperature of each fiber are shown in the figure. The temperature of each measurement is also shown by a thin line.

3.4 X-ray analyses

The WAXD images of all of the drawn fibers showed the α -crystal diffraction features highly oriented along the c axis. The crystallinity index and crystallite size of the drawn fibers were estimated by the peak separation, as well as the case of low molecular weight fibers (m20 and ZN20) [1]. That is, the diffraction angle profile obtained from the diffraction image was averaged along the inclination angle, and the obtained intensity profile was separated into α -crystal diffraction features and an amorphous halo. The crystallinity index (X_{WAXD}) was determined by the ratio of the integrated intensities of the crystal and amorphous phases, and the crystallite size (L_{110}) was also determined by the peak width of (110) diffraction with Scherrer's equation [10]. Both the X_{WAXD} and L_{110} values of m4 and ZN4 showed almost no difference at the same draw ratio. In addition, both X_{WAXD} and L_{110} were almost the same as the values reported for low molecular weight fibers.

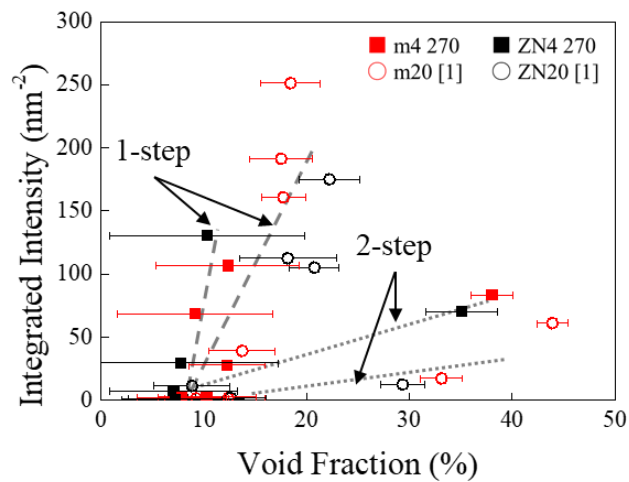
The SAXS image did not show the long-period peak, but it showed the equatorial streak. The equatorial streak originated from the fibrillar structures, i.e., microfibrils and nanoscale voids. The amount of nanoscale voids was determined by the integrated intensity of the equatorial streak, and its correlation length (ζ) was also determined by Debye's equation [11]. Both the void fraction and correlation length began to increase above the whitening draw ratio, but there was almost no difference between the m4 and ZN4 fibers. It has been reported that there is a clear difference in the void fraction at the same integrated intensity between m20 and ZN20 fibers [1]. Therefore, to compare the difference between the m4 and ZN4 fibers, similar to the difference between m20 and ZN20 fibers, the integrated intensity was plotted against the void fraction (V) (**Fig. 3.8**). Assuming a constant fiber density (ρ) of 0.9 g/cm³ [3], because the crystallinities of the drawn fibers were almost the same (**Table 3.3**), V was estimated from the measured (D_{obs}) and calculated (D_{calc}) fiber diameters and the total draw ratio (λ) [1, 12, 13].

$$V = 1 - \frac{1}{\lambda} \left(\frac{D_{\text{calc}}}{D_{\text{obs}}} \right)^2 = 1 - \frac{1}{\lambda} \left(\frac{4W}{\pi\rho v} \cdot \frac{1}{D_{\text{obs}}} \right)^2 \quad (3.1)$$

Table 3.3 Structural parameters of the drawn fibers

Polymer	Drawing	Total Draw		$L_{110}/\mu\text{m}$	X_{WAXD} x100%	$\zeta/\mu\text{m}$	$2R_g/\mu\text{m}$	$d/\mu\text{m}$	$B_0/\text{deg.}$
		Ratio	$V \times 100\%$						
m4*	1-step	10	8	0.010	59	0.002	N/A	N/A	N/A
		12	9	0.010	56	0.008	0.38	5	15
		14	12	0.010	61	0.016	0.38	5	21
	2-step	12	10	0.016	66	0.002	-	-	-
		20	12	0.014	72	0.005	-	-	-
		28	38	0.015	75	0.007	0.76	5	22
ZN4*	1-step	10	7	0.010	54	0.004	-	-	-
		12	8	0.010	56	0.006	-	-	-
		14	10	0.009	58	0.014	0.37	10	21
	2-step	14	8	0.015	66	0.002	-	-	-
		20	7	0.013	72	0.005	-	-	-
		28	35	0.014	78	0.011	-	-	-
m20 [1]	1-step	14	18	0.009	56	0.009	0.34	4	17
ZN20 [1]	1-step	14	18	0.009	57	0.008	-	-	-

*Spinning temperature of 270 °C.

**Fig. 3.8** Integrated intensity of the SAXS equatorial streak plotted against the void fraction estimated from the fiber diameter.

The integrated intensity reflects the amount of 10-nm-order nanoscale voids because the obtained correlation length did not exceed 15 nm. Conversely, even if the void fraction does not consider the void size, the increase of macroscale voids should be dominant in the void fraction above the whitening draw ratio. The difference of the void fraction at the same integrated intensity between the low molecular weight fibers indicates that the molecular weight distribution can influence development of macroscale voids. However, this difference was hardly observed between the high molecular weight fibers. This is probably because of the void fraction being too small to observe the difference in addition to the smaller difference in M_w/M_n . Higher molecular weight should lower the void fraction by suppressing development of macroscale voids.

USAXS images of the drawn fibers are shown in **Fig. 3.9**. Above 12 times drawing of the fibers, equatorial scattering remarkably increased, and the meridional streak could be observed. All of these fibers were whitened. The equatorial scattering can then be assigned to macroscale void development along the fiber axis, and the meridional streak can be assigned to formation of a crack-like scattering body perpendicular to the fiber axis. The crack thickness ($2R_g$) and diameter (d) were estimated from the meridional streak assuming a disk-shaped crack. R_g was determined by Guinier's equation:

$$I(q) = I(0) \exp(-q^2 R_g^2) \quad (3.2)$$

where $I(0)$ is the intensity at $q^2 = 0 \text{ nm}^{-2}$ [14]. d was determined by Ruland's procedure [15]:

$$B_{\text{obs}}^2 = \frac{1}{d^2} \frac{4\pi^2}{q^2} + B_0^2 \quad (3.3)$$

where B_{obs} and B_0 are the integration width along the azimuthal angle and the spread angle indicating the crack inclination. The results of Equation (3.3) are shown in **Fig. 3.10**. A linear relationship was observed for all of the samples.

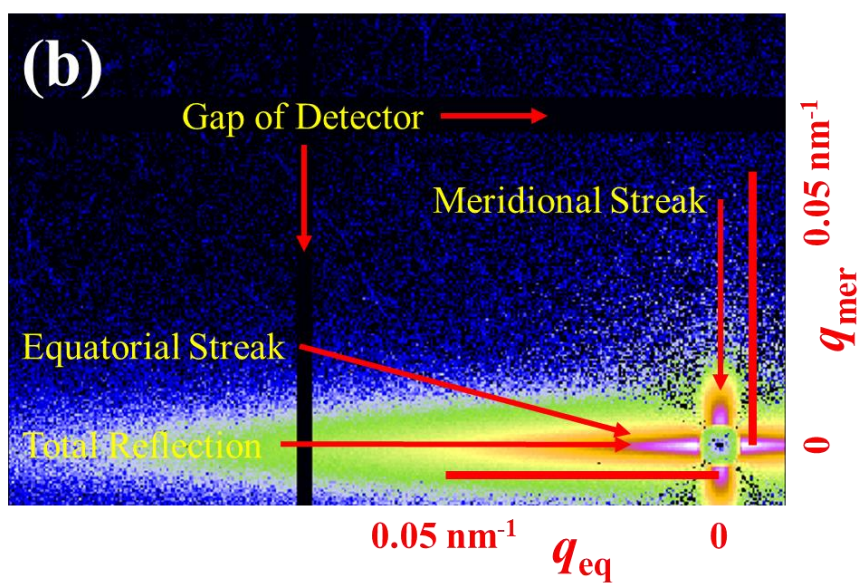
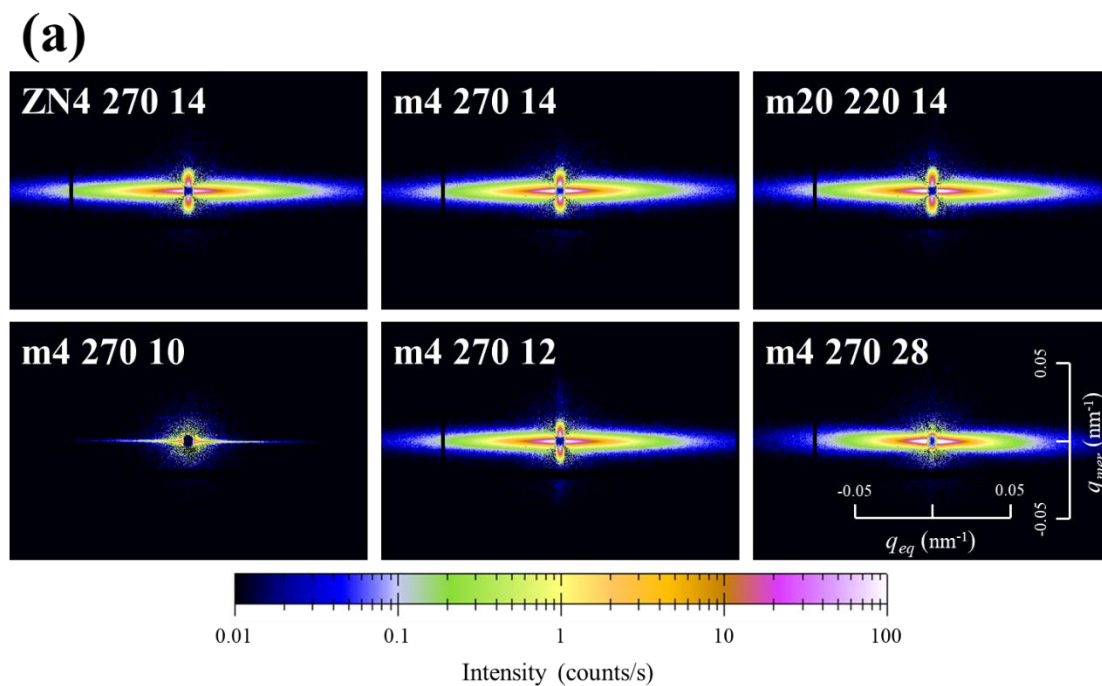


Fig. 3.9 (a) USAXS images of the drawn fibers. The polymer names, spinning temperatures, and total draw ratios are shown in the figures. (b) Typical USAXS image of the m4 fiber spun at 270 °C and drawn 14 times. q_{eq} and q_{mer} indicate the scattering vectors along the equatorial and meridional directions.

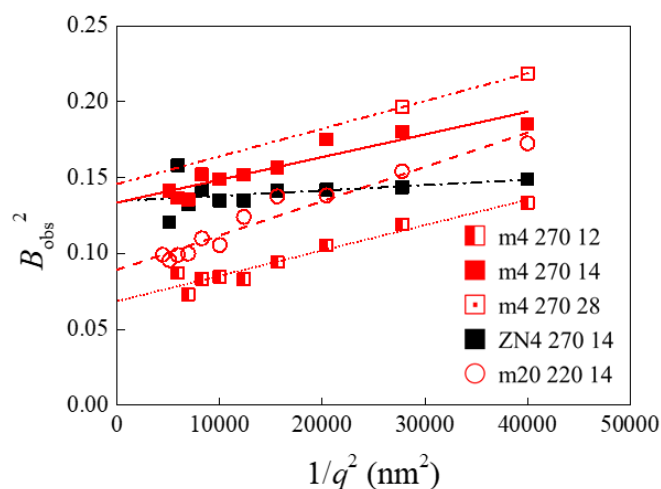


Fig. 3.10 B_{obs} of the USAXS meridional streak plotted against $1/q^2$. The polymer names, spinning temperatures, and total draw ratios are shown in the figure.

The $2R_g$ and d values are given in **Table 3.3**. They were both clearly larger than the correlation length ζ . Therefore, the results obtained by USAXS correspond to the fibril order structure. That is, the obtained crack of several micrometer diameter perpendicular to the fiber axis is thought to be formed between the ends of aligned fibrils. This type of crack has already been reported by Lu et al. [16]. They proposed that the meridional streaks of the USAXS pattern correspond to cracks, which should be formed by separation of the fibril ends. Large crack inclination (B_0) was obtained for the high draw ratio fiber, and large crack thickness ($2R_g$) was obtained for the two-step drawn fiber. This might indicate crack opening with increasing total draw ratio. In addition, the m4 fiber showed a clearly smaller crack diameter (d) than the ZN4 fiber drawn at the same draw ratio. This result suggests that cracks hardly developed in the narrower molecular weight distribution iPP fiber.

Suppression of crack development can explain the high tensile strength of the metallocene catalyst-synthesized iPP fibers. As discussed in Section 3.1, the metallocene catalyst-synthesized iPP as-spun fibers are thought to have a more uniform entangled molecular chain network because of their larger NDR. By drawing the as-spun fiber with a uniform molecular chain network, a uniform fibril structure is likely to form [1]. A model of the fibril structure of each polymer fiber is shown in **Fig. 3.11**. According to the model, a large amount of inter-fibrillar tie-chains could be formed during the drawing process, and the crack development during the drawing process was suppressed for the narrow molecular weight distribution iPP fibers. The larger amount of inter-fibrillar tie-chains could bear more

external force applied to the fiber, and thus the narrow molecular weight distribution iPP fibers have higher tensile strength and smaller creep strain than the wide molecular weight distribution iPP fibers. It has also been reported that higher strength polyethylene terephthalate fiber could be fabricated by drawing as-spun fibers having larger NDR [7, 8, 17].

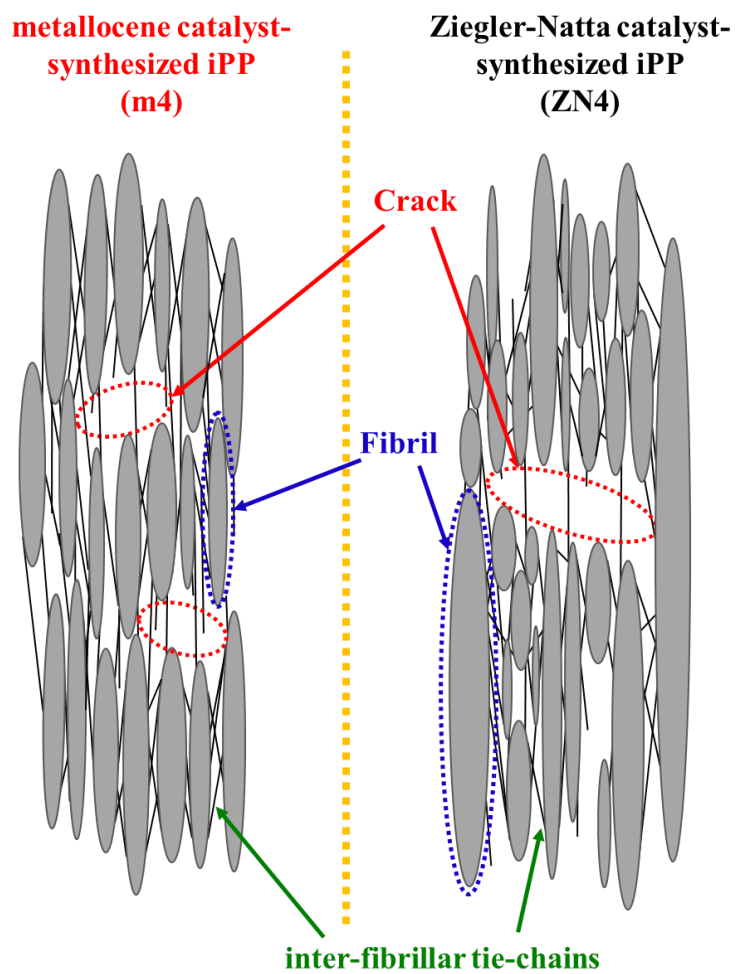


Fig. 3.11 Model of the fibril structure of each polymer fiber.

4. Conclusion

The structure and mechanical properties of fibers produced with high molecular weight metallocene catalyst synthesized iPP have been compared with those of Ziegler–Natta catalyst synthesized iPP and low molecular weight iPPs [1]. To estimate the attainable maximum tensile strength, each polymer was taken up at the lowest possible speed, and the as-spun fibers were drawn to the maximum draw ratio at the highest possible temperature. The mechanical properties and high temperature creep behavior were analyzed, and they were compared with those of fibers fabricated with different polymers. The nanometer to micrometer scale fiber structure was also analyzed by wide, small, and ultra-small angle X-ray measurements. The m4 fibers showed higher tensile strength, higher initial modulus, and lower creep strain at 125 °C than ZN4 fibers. Moreover, higher maximum tensile strength of 1.39 N/tex (1.3 GPa) was obtained for the m4 fibers compared with the m20 fibers. A maximum initial modulus of 26.0 N/tex (23.0 GPa) was also obtained for the m4 fibers. The m4 and m20 fibers also showed smaller crack diameter than that of the ZN4 fibers.

References

- [1] T. Kunimitsu, K. Toyoda, T. Ikaga, K. Kim, Y. Ohkoshi, *Polymer*. 202 (2020) 122654. doi:10.1016/j.polymer.2020.122654.
- [2] K. Koike, Y. Ohkoshi, K. H. Kim, T. Ikaga, T. Kunimitsu, S. Warashina, Japan Patent, Prime Polymer Co., Ltd., Shinshu University, Mitsui Chemicals Inc., P2019-99983 A (2019).
- [3] J. Brandrup, E. H. Immergut, E. A. Grulke, *Polymer Handbook 4th Edition*, John Wiley and Sons, 1999, pp.VI/11. ISBN 0-471-481718-8.
- [4] S. Misra, F.-M. Lu, J. E. Spruiell, G. C. Richeson, *J. Appl. Polym. Sci.* 56 (1995) 1761–1779. doi:10.1002/app.1995.070561307.
- [5] T. Tsutsui, N. Ishimaru, A. Mizuno, A. Toyota, N. Kashiwa, *Polymer*. 30 (1989) 1350–1356. doi:10.1016/0032-3861(89)90059-1.
- [6] S. W. Allison, P. R. Pinnock, I. M. Ward, *Polymer*. 7 (1966) 66–69. doi:10.1016/S0032-3861(66)80018-6.
- [7] T. Kikutani, et al., *Fundamental and Practical Technologies for Nano-Structured Polymeric Materials*, CMC press, 2008, pp.56–110. ISBN 978-4-7813-0043-6.
- [8] R. Tomisawa, S. Oneda, T. Ikaga, K.H. Kim, Y. Ohkoshi, K. Okada, H. Masunaga, T. Kanaya, H. Katsuta, Y. Funatsu, *Polymer*. 164 (2019) 163–173. doi:10.1016/j.polymer.2019.01.002.
- [9] T. Yamashita, *SPRING-8 Section B : Industrial Application Report*. 8 (2020) 368-374. doi:10.18957/rr.8.2.368.
- [10] P. Scherrer, *Göttinger Nachrichten*. 2 (1918) 98–100.
- [11] P. Debye, A. M. Bueche, *J. Appl. Phys.* 20 (1949) 518–525. doi:10.1063/1.1698419.
- [12] Y. A. Kang, X. Zhao, Y. Ohkoshi, K. H. Kim, *Polym. Eng. Sci.* 56 (2016) 609–616. doi:10.1002/pen.24245.
- [13] Y. A. Kang, Y. Ohkoshi, K. H. Kim, *Polym. Plast. Technol. Eng.* 55 (2016) 553–558. doi:10.1080/03602559.2015.1093141.
- [14] A. Guinier, *X-ray Diffraction in Crystals Imperfect Crystals and Amorphous Bodies*, Dover Publications, 1994, pp. 319–350. ISBN 978-0486680118.
- [15] A. F. Thünemann, W. Ruland, *Macromolecules*. 33 (2000) 1848–1852. doi:10.1021/ma991427x.
- [16] Y. Lu, Y. Wang, R. Chen, J. Zhao, Z. Jiang, Y. Men, *Macromolecules*. 48 (2015) 5799–5806. doi:10.1021/acs.macromol.5b00818.
- [17] M. Masuda, W. Takarada, T. Kikutani, *Int. Polym. Process.* 25 (2010) 159–169. doi:10.3139/217.2330.

Chapter 4

Effects of draw ratio and additive on knot-pull
breaking phenomenon in a polypropylene
monofilament

Chapter 4: Effects of draw ratio and additive on knot-pull breaking phenomenon in a polypropylene monofilament

1. Introduction

In this Chapter, I focused on the effects of an acrylic triblock copolymer additive on the knot-pull strength. This additive is usually used as the adhesive, compound, and resin modifier [1], and reportedly increases the toughness of epoxy resin compounds by more than 20 times [2]. Because of the low compatibility between the additive and PP [1], it is also expected that the additive improves the knot-pull strength. To investigate the effects of the additive and the draw ratio on the knot-pull strength of drawn PP monofilaments (thick PP single fibers), the knot-pull strength was compared with the tensile and loop strengths. The broken fiber ends following loop and knot-pull tests were examined using a scanning electron microscope (SEM). The deformation behavior of the knot was also investigated by image processing a video obtained during the knot-pull test.

2 Experimental

2.1 Sample

The PP monofilaments, that is, thick single fiber, used in this study were fabricated by melt-spinning and drawing. Fibers containing 5 wt% additive were also fabricated and compared with the neat PP fibers. The neat PP polymer used for the melt spinning was isotactic polypropylene of Prime Polypro™ (grade Y-2000GV; melt index = 18 g/10 min) supplied by Mitsubishi Chemical Co. (Tokyo, Japan). The additive KURARITY™ (comprising an methyl/n-butyl/methyl acrylic triblock copolymer; grade LA4285; melt index = 31 g/10 min [3]) was also supplied by Mitsubishi Chemical Co. (Tokyo, Japan). The neat polymer was melt-extruded from a BT-30-S 2-42-L twin-screw extruder (Research Laboratory of Plastics Technology Co., Ltd., Tokyo, Japan) using a spinneret with a diameter of 0.7 mm and a length of 2.1 mm. The spinning temperature, mass flow rate, and take-up speed were 220°C, 1.5 g/min, and 100 m/min, respectively. The 5 wt% additive containing PP fiber was also fabricated under the same spinning conditions by mixing a 10 wt% additive containing masterbatch with the neat polymer.

The as-spun fibers were drawn continuously via the speed difference between the feed and take-up rollers. The fiber feed speed was fixed at 1 m/min. A hot plate heater with a contact length of 225 mm set to 140°C was used for drawing. The maximum draw ratio was the draw ratio at which the fiber could be drawn stably for more than 10 min. The drawing tension was measured using a tension meter (HS-1500S, Eiko Sokki Co., Ltd., Osaka Japan) equipped with a 1 N pickup sensor, and the fiber diameter was measured using an outer diameter detector (LS-9006, Keyence Co., Ltd.). Both

measurements were captured by a data logger (NR-2000, Keyence Co., Ltd.) every 100 ms. The drawing stress was calculated from the obtained tension and fiber diameter.

2.2 Thermomechanical property measurements

Differential scanning calorimetry (DSC) was performed using a Thermo Plus DSC 8230 system (Rigaku Co., Ltd.) from room temperature to 200 °C at a rate of 10 K/min. Approximately 2 mg of a cut fiber sample was enclosed in an aluminum pan. Nitrogen gas was supplied at a flow rate of 50 mL/min during the measurement. The melting peak temperature (T_m) and the difference between the heat of fusion and the heat of cold crystallization (ΔH_m) were determined from the DSC curve.

2.3 Tensile test

The tensile test, the loop test, and the knot-pull test were performed for the drawn fibers at room temperature using an Autograph AGS-X instrument (Shimadzu Co., Ltd.) equipped with a 50 N load cell and an air chuck. An overhand knot was selected for the knot-pull test. The tensile strength, loop strength, and knot-pull strength were determined accordingly. The elongation at break and the initial modulus were also determined by the tensile test. Their averages and standard deviations were calculated using at least 12 specimens. The initial crosshead distance was 40 mm, and the elongation speed was 40 mm/min for the drawn fibers. The initial modulus was calculated in the strain range of 0.1%–1.6%. The fiber diameter (d), which was used for all fiber strength calculations, was measured before each test with using a digital microscope (VHX-1000, Keyence Co., Ltd). The samples for the loop and knot-pull tests were prepared so that the loops and knots were located at the midpoints of the chuck.

The broken fiber edges after the loop and knot-pull tests were examined using an SEM (VE9800/8800, Keyence Co., Ltd.). The knot deformation behavior during the knot-pull test was investigated using a digital microscope (VHX-1000, Keyence Co., Ltd), which was equipped with a video camera, and was set on an XYZ axis translation stage. The frame rate was 28 frames/s, and image resolution was 0.95 $\mu\text{m}/\text{pixel}$. During the knot-pull test, the vertical location of the knot was kept in the image by adjusting the microscope height. Still images were extracted from the video using Motion Capture AVI (Digimo Co., Ltd.), and were analyzed using ImageHyper2 (Digimo Co., Ltd.).

3. Result and discussion

3.1 Drawing

The result from the DSC measurements on the as-spun fibers is presented in **Table 4.1**. Both samples had only one melting peak at 167°C.

The drawing stresses are presented in **Fig. 4.1**. The additive reduced the drawing stress at an equivalent draw ratio. It also increased the maximum draw ratio and the whitening draw ratio, at which fiber whitening began. In contrast, the additive had little influence on the whitening stress and maximum drawing stress. These results indicate that the additive acted as a plasticizer in the fiber, that is, it promoted slippage between fibrils. The slippage between fibrils leveled the drawing stress applied to the fibrils, then the slippage increased the whitening draw ratio and the maximum draw ratio, whereas the tolerable maximum drawing stress and the whitening stress were not affected by the slippage.

Table 4.1 Results for the as-spun fibers

Sample	Additive Content (wt%)	Fiber Diameter (μm)	T_m ($^{\circ}\text{C}$)	ΔH_m (J/g)
Neat PP	0	147 ± 5	167	76
Additive-PP	5	147 ± 9	166	70

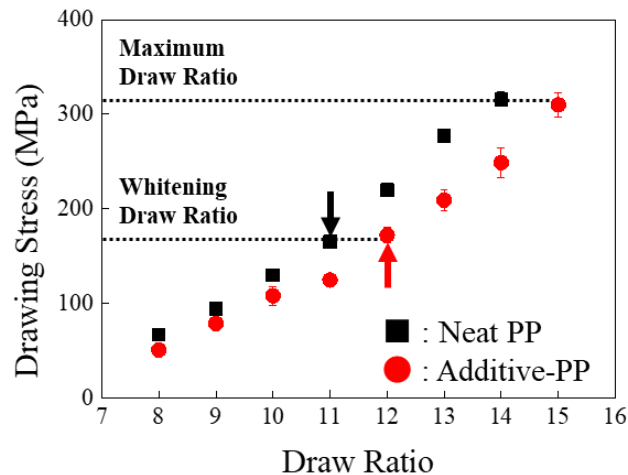


Fig. 4.1 Drawing stress versus draw ratio. The sample markers are defined in the figure, and their whitening draw ratios are indicated by arrows. The whitening and maximum drawing stresses are indicated by dotted lines.

3.2 Mechanical properties

Fig. 4.2 presents the tensile, loop, and knot-pull strengths, whereas Fig. 4.3 and Fig. 4.4 show the initial modulus and elongation at break, respectively. All the fibers were broken at the knot or loop part for each test. The tensile strength and the initial modulus increased, whereas the elongation at break decreased with the draw ratio. The tensile strength of the additive PP fiber increased monotonically up to the maximum draw ratio of the fiber, whereas the tensile strength of neat PP fiber was almost saturated over a draw ratio of 10. Furthermore, as with the increase in the maximum draw ratio, the additive increased the elongation at break for the fiber with the equivalent draw ratio. The loop strength was clearly larger than the tensile strength for a fiber drawn 10 times, while the loop strength was significantly reduced for the maximally drawn fibers. In particular, the loop strength of the additive-containing maximally drawn fiber was obviously lower than its tensile strength. In contrast to the loop strength, the knot-pull strength was constantly lower than the tensile strength over a draw ratio of 8. Furthermore, the additive had no significant effect on the knot-pull strength. That is, although the additive increased the tensile strength of the highly drawn fibers, it did not increase their knot strength.

The additive increased the maximum draw ratio but had little effect on the whitening stress and maximum drawing stress. The additive also increased the tensile strength of the maximally drawn fiber but reduced the tensile strength of the fiber drawn at the lower draw ratio. Low compatibility between the additive and PP has been reported [1], as confirmed by the DSC results described in Section 3.1. Therefore, the PP and additive phases should be separated in the fiber, and the additive—which is dispersed among the PP fibrils—is thought to be stretched by the elongational deformation applied in the spinning and drawing processes. The increase in the maximum draw ratio under the unchanged maximum drawing stress is thought to be caused by slippage at the additive / PP fibril interface with leveling of the stress applied to the fibrils. Stress leveling increased the tensile strength of the highly drawn fibers, whereas the defects formed by slippage at the interface reduced the tensile strength of the low-ratio drawn fibers, because fibrillation was observed at the breaking points of the additive-containing fibers, as shown below. In contrast to the low-ratio drawn fibers, the highly drawn fibers should be fibrillated when they break regardless of the additive. This is because the highly drawn fibers were already whitened by the macroscale voids formed among the fibrils [4]. The fibers should be fibrillated when they break owing to the development of the voids; then, the additive does not reduce the tensile strength of highly drawn fibers, but increases the tensile strength and elongation at break by leveling the stress applied to the PP fibrils.

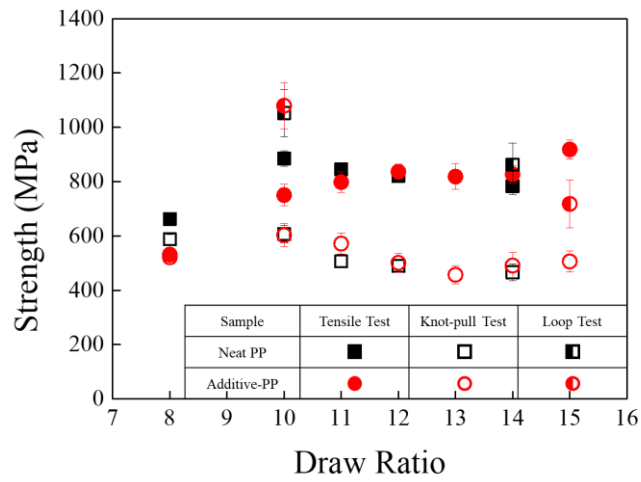


Fig. 4.2 Tensile, loop, and knot-pull strengths of the drawn fibers versus the draw ratio. The sample and test methods are represented in the figure.

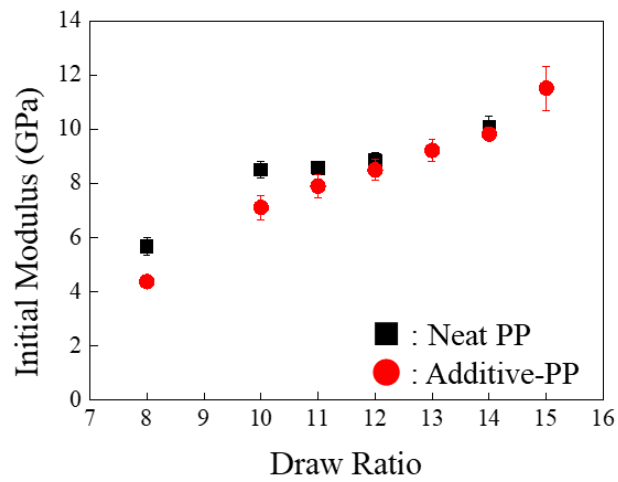


Fig. 4.3 Initial moduli of the drawn fibers versus the draw ratio. The samples are represented in the figure.

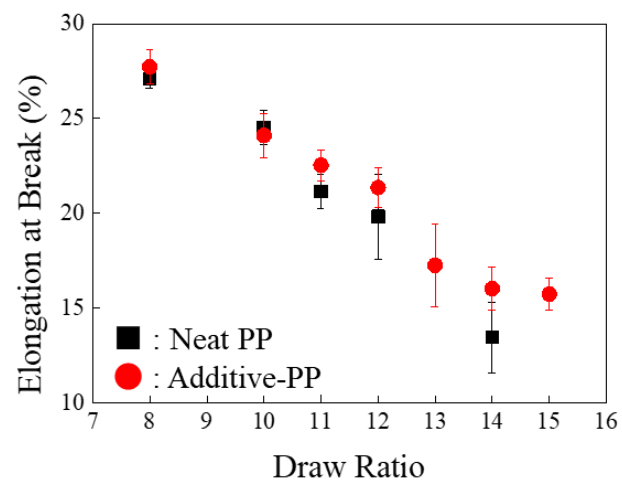


Fig. 4.4 Elongation at break of the drawn fibers versus the draw ratio. The samples are represented in the figure.

Fig. 4.5 shows the SEM images in the vicinity of the fiber breaking point after the loop and knot-pull tests. There was obvious lateral buckling in the surviving side of the fibers after the loop test, particularly in the maximally drawn fibers. However, it is unlikely that the fibers were broken by bending because there were no cracks or kinks perpendicular to the fiber axis on the outside or inside the fibers, respectively. Moreover, there was fibrillation in the broken-side fibers after the loop test, particularly in the additive-containing fibers. This suggests that the maximally drawn fibers were broken with fibrillation at the buckled part.

After the knot-pull test, only one broken end of the 10-times-drawn fiber was buckled, while the other end was not buckled. Furthermore, some knots of the 10-times-drawn PP fiber survived at the broken end. In contrast, both ends of the maximally drawn fibers were buckled. Moreover, the broken ends of the maximally drawn fibers, in particular the additive-containing fibers, were fibrillated. These results suggest that the maximally drawn fibers were broken at the buckled bending part of the knot with fibrillation, as in the loop test, while the 10-times-drawn fiber broke in the vicinity of the knot entrance.

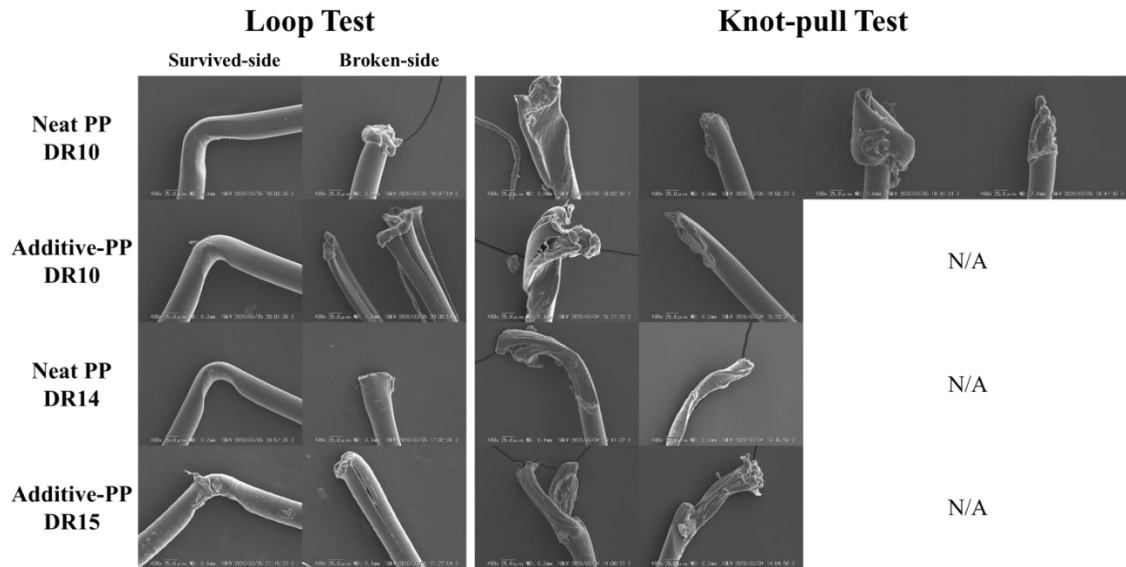


Fig. 4.5 Scanning electron microscope images in the vicinity of the fiber breaking ends and the surviving fiber after the loop and knot-pull tests. The sample and draw ratios are noted in the figure.

3.3 Deformation behavior of the knot

As discussed in Section 3.2, there was a difference between the high-draw-ratio and low-draw-ratio fibers with regard to the fiber breaking mechanism in the knots. A video of the knot deformation behavior until fiber breakage was recorded during the knot-pull tests. The maximally drawn fibers and the 10-times-drawn fibers were selected to represent the high-draw-ratio and low-draw-ratio fibers. The effects of the additive were also examined. The average knot-pull stress-strain curve for these samples were also compared with that of the tensile test, as shown in **Fig. 4.6**. For all samples, the knot-pull stress became lower than the tensile stress at a stress of ~ 100 MPa. **Fig. 4.7** shows still images extracted from the video. The knot seemed to tighten below an applied stress of 100 MPa, and subsequently shrank with increasing applied stress. These results suggested that the knot size decreased mainly by pulling out of the fiber from the knot below 100 MPa, and it decreased mainly by buckling of fiber in the knot above 100 MPa. The knot size of the low-draw-ratio fibers appeared to be larger than that of the high-draw-ratio fibers under an equivalent applied stress. Furthermore, in contrast to the round-shaped knots of the low-draw-ratio fibers, the knots of the high-draw-ratio fibers were somewhat elongated toward the horizontal direction. Both knot shapes became pentagonal under larger applied stresses. However, the change likely occurred at the lower applied stress in the knots of the high-draw-ratio fibers. The pentagonal knots of the high-draw-ratio fibers mainly shrank vertically with the increasing applied stress, whereas those of the low-draw-ratio fibers shrank omnidirectionally. Furthermore, fiber constriction at the knot ends was observed just before the break, which suggests that the radial compressional force was applied at the knot entrance.

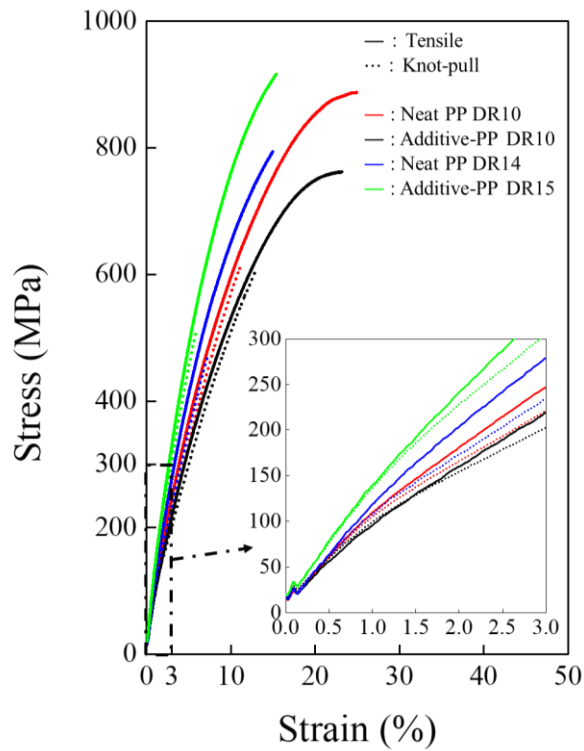


Fig. 4.6 Average stress-strain curve for the tensile (solid line) and knot-pull tests (dotted line). Both strains are defined as the ratio between the change and initial crosshead distance. Enlarged figure is also shown. The sample and draw ratio are noted in the figure.

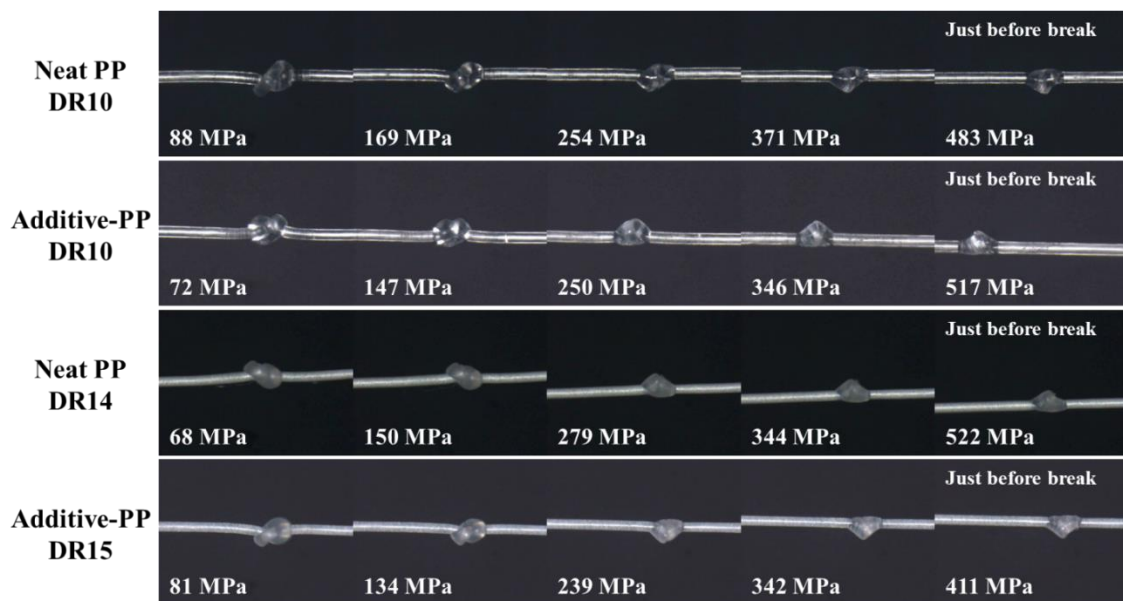


Fig. 4.7 Still images taken in the vicinity of the knot during the knot-pull test. The sample, draw ratio, and each applied stress are noted for each image.

As described above, the knot deformation behavior depended on the fiber sample, in particular the change in size and shape of its knot. Accordingly, the area, length, and thickness of each knot were quantified by applying image processing as follows. First, the diameter profile was obtained from the still image by binarization, blotting out the fiber part, and removing noise using a median filter. The threshold value used for binarization was unified for each test. **Fig. 4.8** shows the typical diameter profile. As shown in the figure, it was possible to obtain the knot length (l) along the fiber axis because there was a clear distinction between the diameter profiles of the knot and fiber. The knot area (a) was obtained by integrating the diameter profile in the range of l , and the average thickness of the knot was obtained by dividing a by l . The normalized knot area (A), the length (L), and the thickness (T) were calculated using equations (4.1) to (4.3) to cancel the effect of the fiber diameter (d):

$$A = \frac{a}{d^2} \quad (4.1)$$

$$L = \frac{l}{d} \quad (4.2)$$

$$T = \frac{A}{L} = \frac{a}{ld} \quad (4.3)$$

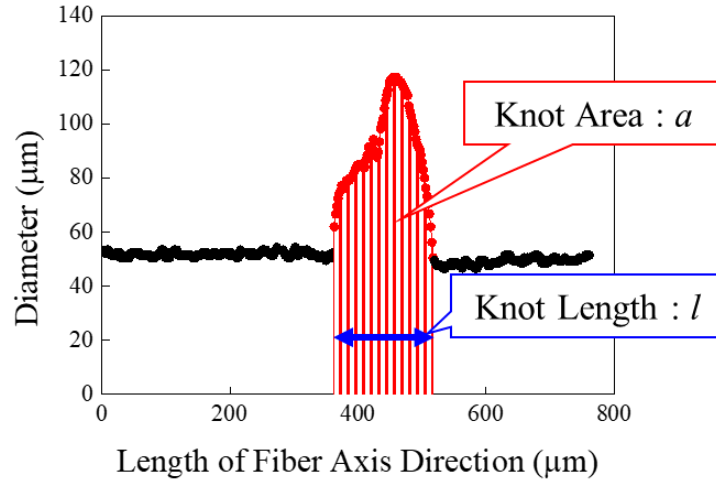


Fig. 4.8 Typical diameter profile in the vicinity of the knot (neat polypropylene (PP) fiber, draw ratio 10). The knot area (a) and length (l) are shown in the figure.

Fig. 4.9 shows the normalized area (A), the length (L), and the average thickness (T) of the knot. The smaller T value of the high-draw-ratio fiber corresponds to the horizontally elongated knot shape, as mentioned above. A , L , and T all decreased until the applied stress reached 200 MPa, which was almost equal to the applied stress at which the knot became pentagonal. At applied stresses over 200 MPa, all the decreases became gentle. However, in contrast to the L and T values of the low-draw-ratio fibers, which both decreased, in the high-draw-ratio fibers only T decreased whereas L did not. The decrease in only T indicated the buckled bending part mainly deformed before breakage. Moreover, as observed in the low-draw-ratio fibers, the decrease in L seemed to be suppressed by the additive.

As demonstrated above, it was possible to quantify the deformation behavior of the knot by image processing, which enabled a clearer representation of the change to the knot shape observed in the videos. However, the shape of a knot cannot be sufficiently expressed by its length and thickness alone. For example, because the knot is cylindrically unsymmetrical, the T value is necessarily affected by the imaging direction, but the L value is not. Owing to the small trial number, there is some level of uncertainty, but there was no clear difference in reproducibility observed between L and T in the present study, which indicates that the imaging direction had little influence on reproducibility. More detailed analysis can be expected from a greater trial number and a higher image resolution.

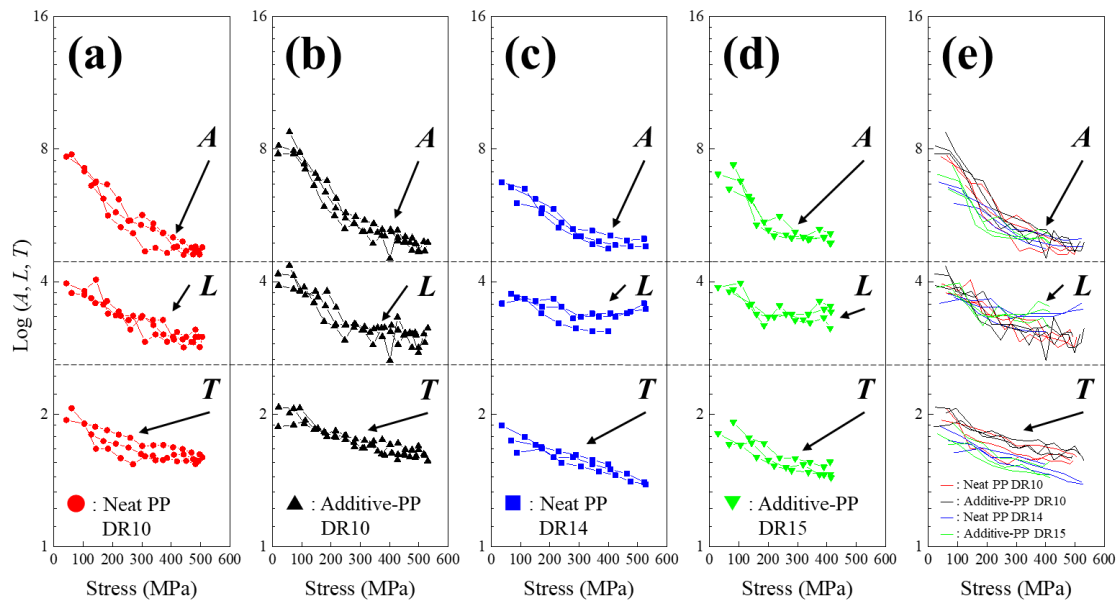


Fig. 4.9 Normalized knot area (A), knot length (L), and knot thickness (T) obtained by the knot shape image taken during the knot-pull test versus the stress applied at the time. Neat PP (a, c) and additive-PP (b, d) fibers were drawn to 10 (a, b), 14 (c), and 15 (d) times. The data are superimposed in (e).

3.4 Fiber breaking mechanism of the knot

Many kinds of force are applied to a knotted fiber, including tensile, bending, compressional, twisting, shearing, and frictional forces [5, 6]. Among them, the effects of twisting and shearing on knotted fiber breakage are reportedly small [7, 8]. Two dominant fiber breaking forms were observed for the overhand knot in the present study, that is, tensile breakage resulting from the normal stress difference between the tensile force and the radial compressional force, and fiber breakage with buckling and fibrillation resulting from the lateral compressional force (**Fig. 4.10**). That is, the low-draw-ratio fibers broke in the vicinity of the knot entrance as a result of the tensile force, whereas the high-draw-ratio fibers broke at the buckled bending part in the knot with fibrillation as a result of the lateral compressional force. In contrast, the contribution of twisting and shearing forces to knot breakage was limited, as observed in the SEM images.

The stress field of the knotted fiber is expressed by equation (4.4). As shown in the equation, the tensile stress (σ_{zz}) and radial compressional stress ($-\sigma_r$) arise normal to the stress difference $\sigma_{zz} + \sigma_r$ and hydrostatic pressure $(\sigma_{zz} - \sigma_r)/3$.

$$\begin{pmatrix} -\sigma_r & 0 & 0 \\ 0 & -\sigma_r & 0 \\ 0 & 0 & \sigma_{zz} \end{pmatrix} = \frac{1}{3} \left\{ \begin{pmatrix} -\sigma_{zz} - 2\sigma_r & 0 & 0 \\ 0 & -\sigma_{zz} - 2\sigma_r & 0 \\ 0 & 0 & 2\sigma_{zz} + \sigma_r \end{pmatrix} + (\sigma_{zz} - \sigma_r) \begin{pmatrix} 1 & 0 & 0 \\ 0 & 1 & 0 \\ 0 & 0 & 1 \end{pmatrix} \right\} \quad (4.4)$$

The tensile breaking stress of the knotted fiber should be lowered by the tensile strength as much as the radial compressional force σ_r . In contrast, the fibrillation of the knotted fiber should be suppressed by the hydrostatic pressure $\sigma_r/3$ compared with that occurring in the loop test. In addition, the buckling and fibrillation are suppressed by fiber friction, which reduces the lateral compressional force.

The low-draw-ratio fibers had larger loop strengths than tensile strengths. This indicates that the fiber in the knot did not break by buckling but broke because of the tensile force. This tensile breakage was promoted by the increase in the normal stress difference by as much as σ_r . The normal stress difference is highest at the knot entrance where the tensile force is not reduced by the frictional force acting between the fibers in the knot. Moreover, the continuous decrease of knot area A indicates the monotonical increase of σ_r until fiber breakage. Therefore, the low-draw-ratio fiber likely broke as a result of the normal stress difference between σ_{zz} and σ_r . Unlike the low-draw-ratio fibers, there was little difference between the loop and tensile strengths in the high-draw-ratio fibers, which indicates that the fibers did not break as a result of the normal stress difference. The high-draw-ratio fibers, which had already whitened, were easily fibrillated, as observed in the broken fiber ends resulting

from the loop and knot-pull tests that were fibrillated. The fiber breakage within the knots also suggested fiber breakage at the buckled part. The decrease of only T , as described in Section 3.3, also confirmed that the deformation was concentrated in the buckled bending part before breakage. Therefore, the high-draw-ratio fibers likely broke at the buckled part in the knot with fibrillation because of lateral compressional force.

The effect of the additive was observed in the broken fiber ends, particularly those from the loop test. The broken ends of the additive-containing fibers were fibrillated regardless of the draw ratio. This suggests that the additive promoted fibrillation. Fibrillation was further promoted in the high-draw-ratio fibers. The fibrillation promotion effect of the additive explains the relatively low knot-pull strength of the additive containing high-draw-ratio fibers, despite their higher tensile strength. The fibrillation promotion effect also explains the relatively low tensile strength of the additive containing low-draw-ratio fibers, which could be ascertained by their fibrillated broken ends, as observed via SEM. Nevertheless, the additive did not reduce the knot-pull strength of the low-draw-ratio fibers because the increase in hydrostatic pressure by as much as $\sigma_r/3$ likely cancelled the fibrillation promotion effect.

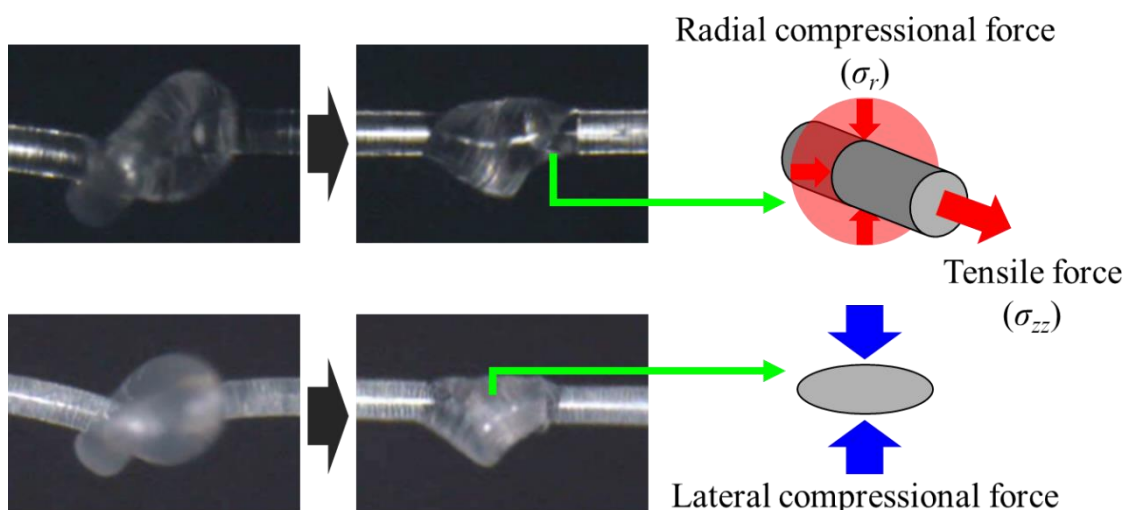


Fig. 4.10 Typical micro-images taken during the knot-pull test. The images correspond to stresses lower than 100 MPa and those immediately before the break. The low-draw-ratio neat polypropylene (PP) fibers of draw ratio 10 and the high-draw-ratio additive-containing PP fibers of draw ratio 15 are shown in the upper and lower rows, respectively. Major forces applied to the knot are also illustrated.

4. Conclusion

To investigate the breaking mechanism of knotted PP monofilament, that is, thick single fiber, the knot-pull, tensile, and loop strengths were evaluated for neat and additive-containing PP fibers fabricated by melt-spinning and drawing. The broken fiber ends resulting from the loop and knot-pull tests were examined via SEM. The deformation behavior of the knot during the knot-pull test was also investigated.

The knot-pull strength was constantly lower than the tensile and loop strengths. In contrast, the loop strength of the low-draw-ratio fibers was clearly larger than the tensile strength, but largely decreased in the high-draw-ratio fibers. The SEM revealed two forms of broken fiber ends: the low-draw-ratio fibers, which were broken at the knot entrance, hardly produced buckled fiber ends, whereas the high-draw-ratio fibers, which were broken within the knot, produced buckled and fibrillated fiber ends. The tendency observed for the high-draw-ratio fibers was confirmed by image analysis of the video obtained during the knot-pull test. That is, the knot thickness of the high-draw-ratio fiber continued to decrease until fiber breakage, even after the knot length stopped decreasing. This indicates that fiber buckling occurred before fiber breakage. Therefore, the low-draw-ratio fiber likely broke as a result of the normal stress difference, whereas the high-draw-ratio fiber probably broke at the buckled part in the knot with fibrillation as a result of lateral compressional force.

The additive increased the tensile strength, particularly in the high-draw-ratio fibers, whereas it barely affected the knot-pull strength. The additive probably leveled the stress applied to the fibrils, but it also promoted fibrillation in the fiber. The knot-pull strength hardly increased because the promotion effect was likely cancelled by the tensile strength increase. The promotion effect also reduced the tensile strength of the low-draw-ratio fibers, but the knot-pull strength was not reduced. This was because fibrillation seemed to be suppressed by the increase in hydrostatic pressure.

References

- [1] T. Ono, Journal of The Adhesion Society of Japan. 52 (2016) 342–347.
doi:10.11618/adhesion.52.342.
- [2] H. Kishi, Y. Kunimitsu, J. Imade, S. Oshita, Y. Morishita, M. Asada, Polymer. 52 (2011) 760–768. doi:10.1016/j.polymer.2010.12.025.
- [3] KURARITY™ Acrylic Block Copolymer Technical information
https://www.kuraray.com/uploads/5e4f6cdf20d15/Kurarity_technical_brochure_en.pdf.
(accessed 15 June 2020)
- [4] T. Kunimitsu, K. Toyoda, T. Ikaga, K. Kim, Y. Ohkoshi, K. Koike, Polymer. 202 (2020) 122654.
doi:10.1016/j.polymer.2020.122654.
- [5] R. Oono, Journal of Home Economics of Japan. 47 (1996) 461–468.
doi:10.11428/jhej1987.47.461.
- [6] H. Endo, S. Ohira, Seni binran 3rd edition, Sen'i Gakkai Ed., Maruzen Publishing, 2004, pp.55–56. ISBN 978-4-621-07485-5.
- [7] H. Yabe, Journal of Chugoku Junior College. 18 (1987) 1–8.
- [8] A. Konda, C. Koyama, T. Agatsuma, Bulletin of the Textile Research Institute, 62 (1962) 25–29.

Chapter 5

Conclusions

Chapter 5: Conclusions

Recently, a high stereoregularity isotactic polypropylene (iPP) has been synthesized with the use of metallocene catalysts. In this study, the attainable maximum tensile strength of this metallocene catalyst-synthesized iPP fiber with 20 g/10 min and 4 g/10min melt index was evaluated. Moreover, the effects of the molecular weight distribution and stereoregularity of iPP on the structure and properties of its fibers were also analyzed by comparison between that of Ziegler–Natta catalyst-synthesized iPP with equivalent stereoregularity and low stereoregularity metallocene catalyst-synthesized iPP. In addition, as well as tensile strength, knot-pull strength is also important, but the mechanism by which the fiber in a knot breaks has not been sufficiently elucidated. Therefore, the effects of the draw ratio and a melt-kneaded additive on the knot-pull strength and knot-pull breaking mechanism of iPP monofilament, that is, a thick single fiber, were also discussed in this study.

In Chapter 2, the effects of iPP stereoregularity and molecular weight distribution on the properties and structure of fibers were investigated for metallocene catalyst-synthesized iPP with an isotactic pentad fraction (IPF) of 98% and Mw/Mn 2.5, metallocene catalyst-synthesized iPP with an IPF of 93% and Mw/Mn 2.5, and a Ziegler–Natta catalyst-synthesized iPP with an IPF of 98% and Mw/Mn 3.5. The fibers were obtained by melt spinning, and drawn twice. To compare the attainable maximum tensile strength, each polymer fiber was taken-up at the minimum stable melt draw ratio, and the as-spun fibers were drawn to the maximum draw ratio at the drawable maximum temperature for each polymer. The high stereoregularity metallocene catalyst-synthesized iPP clearly contributed to greater tensile strength and initial modulus. These results are explained by the greater maximum draw ratio, crystallinity, and crystallite size. These factors are all related to the higher drawing temperature that is achievable because of the higher melting temperature. As a result, the maximum tensile strength of 1.36 N/tex (~1.2 GPa) and a maximum initial modulus of 27.4 N/tex (~25 GPa) were obtained for high stereoregularity metallocene catalyst-synthesized iPP fiber drawn over 20 times. The high stereoregularity metallocene catalyst-synthesized iPP fibers also indicated a higher birefringence and a greater drawing stress than those of the Ziegler–Natta catalyst-synthesized iPP fiber at the same draw ratio. Moreover, the metallocene catalyst-synthesized iPP fiber having almost the same tensile strength of Ziegler–Natta catalyst-synthesized iPP fibers also had a lower creep strain at 125 °C under 50-MPa tensile stress. There was almost no difference in the crystalline dispersion temperature, melting temperature, crystallinity, and crystallite size observed between the drawn fibers of different catalyst iPP spun and drawn under the same conditions; however, the tensile strength of the metallocene catalyst-synthesized iPP drawn fiber decreased less for a total draw ratio greater than 14 than did the Ziegler–Natta catalyst-synthesized iPP fiber, which contributed to a higher attainable maximum tensile strength of the metallocene catalyst-synthesized iPP fiber. The fibrillation at fracture and whitening were also suppressed for metallocene catalyst-synthesized iPP. Furthermore,

macroscale void formation, estimated by the fiber diameter, in the Ziegler–Natta catalyst-synthesized iPP fiber was more pronounced than that in the metallocene catalyst-synthesized iPP fiber having an equivalent amount of nanoscale voids (~10 nm) estimated from the equatorial streak of the SAXS. The lower content of macroscale voids form in the drawing of the metallocene catalyst-synthesized iPP fibers was consistent with the suppressed fibrillation tendency at fracture.

In Chapter 3, the structure and mechanical properties of fibers produced with high molecular weight (melt index of 4 g/10 min) metallocene catalyst-synthesized iPP have been compared with those of Ziegler–Natta catalyst synthesized iPP and low molecular weight iPPs. To estimate the attainable maximum tensile strength, each polymer was taken up at the lowest possible speed, and the as-spun fibers were drawn to the maximum draw ratio at the highest possible temperature. The mechanical properties and high temperature creep behavior were analyzed, and they were compared with those of fibers fabricated with different polymers. The nanometer to micrometer scale fiber structure was also analyzed by wide, small, and ultra-small angle X-ray measurements. The high molecular weight metallocene catalyst-synthesized iPP fibers showed higher tensile strength, higher initial modulus, and lower creep strain at 125 °C than Ziegler–Natta catalyst synthesized iPP fibers. Moreover, higher maximum tensile strength of 1.39 N/tex (1.3 GPa) was obtained for the high molecular weight metallocene catalyst-synthesized iPP fibers compared with the low molecular weight metallocene catalyst-synthesized iPP fibers. A maximum initial modulus of 26.0 N/tex (23.0 GPa) was also obtained for the high molecular weight metallocene catalyst-synthesized iPP fibers. The both molecular weight metallocene catalyst-synthesized iPP fibers also showed smaller crack diameter than that of the high molecular weight Ziegler–Natta catalyst synthesized iPP fibers.

From Chapter 2 and 3, the higher tensile strength of narrow molecular weight distribution iPP should be explained by the suppression of macroscale voids formation and crack development, which should be brought by the more uniform molecular chain network. The lower creep strain at high temperature is also explained by the uniform molecular chain network.

In Chapter 4, to investigate the breaking mechanism of knotted iPP monofilament, that is, thick single fiber, the knot-pull, tensile, and loop strengths were evaluated for neat and additive-containing PP fibers fabricated by melt-spinning and drawing. The broken fiber ends resulting from the loop and knot-pull tests were examined via SEM. The deformation behavior of the knot during the knot-pull test was also investigated. The knot-pull strength was constantly lower than the tensile and loop strengths. In contrast, the loop strength of the low-draw-ratio fibers was clearly larger than the tensile strength, but largely decreased in the high-draw-ratio fibers. The SEM revealed two forms of broken fiber ends: the low-draw-ratio fibers, which were broken at the knot entrance, hardly produced buckled fiber ends, whereas the high-draw-ratio fibers, which were broken within the knot, produced buckled and fibrillated fiber ends. The tendency observed for the high-draw-ratio fibers was confirmed by image analysis of the video obtained during the knot-pull test. That is, the knot thickness of the high-

draw-ratio fiber continued to decrease until fiber breakage, even after the knot length stopped decreasing. This indicates that fiber buckling occurred before fiber breakage. Therefore, the low-draw-ratio fiber likely broke as a result of the normal stress difference, whereas the high-draw-ratio fiber probably broke at the buckled part in the knot with fibrillation as a result of lateral compressional force. The additive increased the tensile strength, particularly in the high-draw-ratio fibers, whereas it barely affected the knot-pull strength. The additive probably leveled the stress applied to the fibrils, but it also promoted fibrillation in the fiber. The knot-pull strength hardly increased because the promotion effect was likely cancelled by the tensile strength increase. The promotion effect also reduced the tensile strength of the low-draw-ratio fibers, but the knot-pull strength was not reduced. This was because fibrillation seemed to be suppressed by the increase in hydrostatic pressure.

Publications

The dissertation is based on the following published papers.

Journal of articles

- Tatsuma Kunimitsu, Kai Toyoda, Toshifumi Ikaga, KyoungHou Kim, Yutaka Ohkoshi, Katsuhiko Koike, High strength fiber obtained from a high stereoregularity metallocene catalyst-synthesized polypropylene, *Polymer*, 202, 122654 (2020)
- Tatsuma Kunimitsu, Chisa Ikeda, Shuntaro Oshima, Toshifumi Ikaga, KyoungHou Kim, Yutaka Ohkoshi, Masayuki Takata, Tomoyoshi Yamashita, Effects of Draw Ratio and Additive on Knot-Pull Breaking Phenomenon in a Polypropylene Monofilament, *Journal of Fiber Science and Technology*, 76, 403 – 411 (2020)
- Tatsuma Kunimitsu, Shuji Warashina, Toshifumi Ikaga, KyoungHou Kim, Yutaka Ohkoshi, Katsuhiko Koike, High Strength Metallocene Catalyst-Synthesized Polypropylene Fibers with High Stereoregularity and High Molecular Weight, *Journal of Fiber Science and Technology*, 77, 66 – 75 (2021).

Conferences

A part of the dissertation was presented in conferences as the following.

Oral presentations

- 平成 29 年度繊維学会年次大会: 國光立真、豊田海、伊香賀敏文、金慶孝、大越豊、小池勝彦、分子量分布がアイソタクチックポリプロピレン水冷紡糸繊維の力学物性および熱機械物性におよぼす影響
- The 14th Asian Textile Conference: Tatsuma Kunimitsu, Kai Toyoda, Toshifumi Ikaga, KyoungHou Kim, Yutaka Ohkoshi, Katsuhiko Koike, Effects of molecular weight distribution and stereoregularity on the properties and structure of Isotactic Polypropylene fiber
- The 12th SPSJ International Polymer Conference: Tatsuma Kunimitsu, Shuji Warashina, Toshifumi Ikaga, KyoungHou Kim, Yutaka Ohkoshi, Katsuhiko Koike, Effect of molecular weight and its distribution on the properties and structure of polypropylene fiber

Poster presentations

- 平成 28 年度繊維学会年次大会: 國光立真、豊田海、伊香賀敏文、金慶孝、大越豊、小池勝彦、分子量分布と立体規則性がアイソタクチックポリプロピレン (iPP) 繊維の物性と構造に及ぼす影響
- The 32nd International Conference of the POLYMER PROCESSING SOCIETY: Tatsuma Kunimitsu, Kai Toyoda, Toshifumi Ikaga, KyoungHou Kim, Yutaka Ohkoshi, Katsuhiko Koike, Effects of molecular weight distribution and stereoregularity on mechanical properties and structure of Isotactic Polypropylene (iPP) fiber
- The 15th Asian Textile Conference: Tatsuma Kunimitsu, Chisa Ikeda, Shuntaro Oshima, Toshifumi Ikaga, KyoungHou Kim, Yutaka Ohkoshi, Masayuki Takata, Tomoyoshi Yamashita, Effects of additives on the tensile and knot-pull strength of polypropylene fibers

Acknowledgments

本論文は筆者が信州大学大学院総合医理工学研究科総合理工学専攻に在籍中の研究成果をまとめたものであります。信州大学繊維学部教授大越豊先生には、指導教官として本研究の実施の機会を与えていただき、その遂行にあたって終始、ご指導いただきました。ここに深謝の意を表します。信州大学繊維学部教授金慶孝先生、並びに信州大学繊維学部教授石澤広明先生には副指導教官として研究のご助言をいただきました。ここに深謝の意を表します。東京工業大学物質理工学院特任教授鞠谷雄士先生には本論文の執筆にあたりご指導ご鞭撻を賜りましたこと、ここに厚く御礼申し上げます。North Carolina State University, Associate Professor Richard Kotek 先生には海外留学の受け入れ、貴重な研究の機会を与えてくださったこと、ここに深く御礼申し上げます。

本研究を進めるにあたり、研究テーマの提案や樹脂の提供、論文執筆の際の有益なご討論ご助言をいただきました株式会社プライムポリマー/三井化学株式会社小池勝彦博士、三菱ケミカル株式会社山下友義博士、同株式会社高田昌幸氏にも深く御礼申し上げます。紡糸・延伸実験をサポートいただきました信州大学繊維学部技術職員伊香賀敏文技官、岡田祐輔技官、武藤雄一技官、並びに菅原昂亮技官にも心より感謝申し上げます。また日頃の実験や結果考察の際に、有益なご討論ご協力をいただきました信州大学大学院理工学系研究科繊維・感性工学専攻修士豊田海氏、信州大学大学院総合理工学研究科繊維学専攻修士池田知紗氏、同専攻修士藁科修治氏、並びに、同専攻修士大島竣太郎氏にも厚く御礼申し上げます。

本論文は、信州大学繊維学部博士課程教育リーディングプログラム「ファイバールネッサンスを先導するグローバルリーダーの養成」の支援を受けました。また、超小角 X 線散乱測定は、大型放射光施設 SPring-8 BL19B2 で実施されました。